

Reconstructed Density and Velocity Fields from the 2MASS Redshift Survey

Pirin Erdoğdu^{1,2,3}, Ofer Lahav^{3,4}, John P. Huchra^{5*}, Matthew Colless⁶, Roc M. Cutri⁷, Emilio Falco^{5*}, Teddy George⁶, Thomas Jarrett⁸, D. Heath Jones⁷, Lucas M. Macri⁹, Jeff Mader¹⁰, Nathalie Martimbeau⁵, Michael A. Pahre⁵, Quentin A. Parker^{7,11}, Anaïs Rassat⁴, Will Saunders⁷

¹ Department of Physics, Middle East Technical University, 06531, Ankara, Turkey

² School of Physics & Astronomy, University of Nottingham, University Park, Nottingham, NG7 2RD, UK

³ Institute of Astronomy, Madingley Road, Cambridge, CB3 0HA, UK

⁴ Department of Physics and Astronomy, University College London, Gower Street, London WC1E 6BT, UK

⁵ Harvard-Smithsonian Centre for Astrophysics, 60 Garden Street, MS-20, Cambridge, MA 02138, USA

⁶ Canada-France-Hawaii Telescope Corporation, 65-1238 Mamalahoa Hwy Kamuela, Hawaii 96743, USA

⁷ Anglo-Australian Observatory, PO Box 296, Epping, NSW 2052, Australia

⁸ Infrared Processing and Analysis Center, California Institute of Technology, Pasadena, CA 91125, USA

⁹ National Optical Astronomy Observatory, 950 North Chry Avenue, Tucson, AZ 85726, USA

¹⁰ W.M. Keck Observatory, Kamuela, HI 96743, USA

¹¹ Department of Physics, Macquarie University, Sydney, NSW 2109, Australia

* Guest Observer, Cerro Tololo Interamerican Observatory, operated by AURA for the National Science Foundation

20 May 2021

ABSTRACT

We present the reconstructed real-space density and the predicted velocity fields from the Two Mass Redshift Survey (2MRS). The 2MRS is the densest all-sky redshift survey to date and includes about 23,200 galaxies with extinction corrected magnitudes brighter than $K_s = 11.25$. Our method is based on the expansion of these fields in Fourier-Bessel functions. Within this framework, the linear redshift distortions only affect the density field in the radial direction and can easily be deconvolved using a distortion matrix. Moreover, in this coordinate system, the velocity field is related to the density field by a simple linear transformation. The shot noise errors in the reconstructions are suppressed by means of a Wiener filter which yields a minimum variance estimate of the density and velocity fields. Using the reconstructed real-space density fields, we identify all major superclusters and voids. At $50 h^{-1}$ Mpc, our reconstructed velocity field indicates a back-side infall to the Great Attractor region of $v_{\text{infall}} = (491 \pm 200)(\beta/0.5) \text{ km s}^{-1}$ in the Local Group frame and $v_{\text{infall}} = (64 \pm 205)(\beta/0.5) \text{ km s}^{-1}$ in the cosmic microwave background (CMB) frame and β is the redshift distortion parameter. The direction of the reconstructed dipole agrees well with the dipole derived by Erdoğdu *et al.* (2006). The misalignment between the reconstructed 2MRS and the CMB dipoles drops to 13° at around 5000 km s^{-1} but then increases at larger distances.

Key words: astronomical data bases:surveys–cosmology: observations – large-scale structure of universe – galaxies: distances and redshifts

1 INTRODUCTION

A cosmographical description of the galaxy distribution is crucial to our understanding of the mechanisms of structure formation that generate the complex pattern of sheets and filaments comprising the ‘cosmic web’. Today, there are many more redshifts available for galaxies than velocity measurements. This discrepancy has in-

spired a great deal of work on methods for the reconstruction of the mass and velocity fields from redshifts alone. These methods use a variety of functional representations (e.g. Cartesian, Fourier, spherical harmonics or wavelets) and smoothing techniques (e.g. a Gaussian or a top-hat sphere). However, several complications arise when one tries to reconstruct peculiar velocity and real-space mass density fields directly from redshift surveys. First, one must

relate the light distribution to the mass field. On large scales, this relationship is generally assumed to be linear with a proportionality constant (but see e.g. Wild *et al.* 2005; Conway *et al.* 2005; Marinoni *et al.* 2005 who argue that biasing is non-linear and redshift dependent even on large scales). Another common assumption is that the galaxy distribution samples the underlying smooth mass field and the finite sampling of the smooth field introduces Poisson ‘shot noise’ errors¹. Yet another important physical problem associated with the recovery of the real-space mass density field from the galaxy density field is the correction of the distortions in the redshift space clustering pattern. Furthermore, in redshift surveys the actual number of galaxies in a given volume is larger than the number observed, particularly in flux limited samples where at large distances only the very luminous galaxies can be seen.

In this paper, we recover the real-space density and predicted velocity fields of the 2MRS (Huchra *et al.* 2005). The reconstruction procedure used is based on linear theory and closely follows Fisher *et al.* (1995, hereafter FLHLZ). The density field in redshift-space is decomposed into spherical harmonics and Bessel functions (*Fourier-Bessel functions*). Then the real-space density and velocity fields are reconstructed from those in the redshift-space using a Wiener filter.

The idea of cosmography using spherical harmonics goes back to Peebles (1973) but the method only gained popularity with the advent of all-sky surveys. Since then, it has been applied to the Infrared Astronomical Satellite (*IRAS*) selected galaxy surveys (e.g. to the *IRAS* 1.2 Jy Survey by Fabbri & Natale 1990; Scharf *et al.* 1992; Scharf & Lahav 1993; Fisher, Scharf & Lahav 1994; Lahav *et al.* 1994; Nusser & Davis 1994; Heavens & Taylor 1995 and to *IRAS* Point Source Catalogue Redshift Survey (PSCz) by Tadros *et al.* 1999, Hamilton, Tegmark & Padmanabhan 2000; Taylor *et al.* 2001) and the peculiar velocity catalogues (e.g. to elliptical galaxy sample by Regös & Szalay 1989; to Mark III galaxy sample by Davis, Nusser & Willick 1996 and Hoffman *et al.* 2001). The spherical harmonics technique has proven to be very convenient for addressing many of the problems inherent to the analyses of redshift surveys. The spherical harmonics are one of the most convenient ways of smoothing the noisy data. A careful choice of spherical coefficients greatly reduces the statistical uncertainties and errors introduced by the non-linear effects. Furthermore, the treatment of linear redshift distortions are particularly straightforward in Fourier-Bessel space, especially for surveys which have almost all-sky coverage and dense sampling such as 2MRS.

The Wiener-filtered fields are optimal reconstructions in the sense that the variance between the derived reconstruction and the underlying true field is minimised. As opposed to *ad hoc* smoothing schemes, the smoothing due to the Wiener filter is determined by the data. In the limit of high signal-to-noise, the Wiener filter modifies the observed data only weakly, whereas it strongly suppresses the contribution of the data contaminated by shot noise. The three-dimensional Wiener reconstruction of cosmological fields in Fourier-Bessel space was first developed by FLHLZ and applied to the *IRAS* 1.2 Jy survey. Webster *et al.* (1997, hereafter WLF) expanded on the initial results of FLHLZ. Later, Schmoldt *et al.*

(1999) applied the same method to the *IRAS* PSCz survey to recover density and velocity fields.

This paper is structured as follows: in the next section, we describe the Two Micron Redshift Survey. In Section 3, we give a brief summary of the decomposition of the density field in redshift-space into a set of orthogonal spherical harmonics and Bessel functions. In Section 4, we discuss how these redshift-space harmonics are related to those in real-space. In Section 5, we give expressions for the Wiener filter in Fourier-Bessel space. The implementation of the method to 2MRS is given in Section 6, along with the maps of the density and velocity fields. In the same section, we also show reconstruction of the Local Group (LG) acceleration determined directly from harmonic coefficients. The last section contains a discussion and summary of the work. Throughout this paper, we assume that the galaxy distribution is related to the underlying smooth mass density field by the linear bias parameter, b , so that $\delta_g(\mathbf{x}) = b\delta_m(\mathbf{x})$. With this notation, the constant of proportionality between velocity and the density field is β , where $\beta = \Omega_m^{0.6}/b$. It is worth emphasising that one of the ultimate goals of this work is to test linear biasing by comparing the reconstructed velocity fields with the observed peculiar velocity field. The distances are given in units of velocity and the Hubble constant is $H_0 = 100 h \text{ kms}^{-1} \text{ Mpc}^{-1}$.

2 THE TWO MICRON ALL-SKY REDSHIFT SURVEY

The Two Micron All-Sky Redshift Survey (2MRS) is the densest all-sky redshift survey to date. The galaxies in the northern celestial hemisphere are being observed by the Fred Lawrence Whipple Observatory (FLWO) 1.5-m telescope, the Arecibo 305-m telescope and the Green Bank 100-m Telescope. In the southern hemisphere, most galaxies at high galactic latitude (about 6000 galaxies) were observed as a part of the 6-degree field galaxy survey² (6dFGS, Jones *et al.* 2004; Jones *et al.* 2005) and the low galactic latitude galaxies are being observed at CTIO (by L. Macri and J.P. Huchra). The first phase of 2MRS is now complete. In this phase we obtained redshifts for approximately 23,150 2MASS galaxies from a total sample of 24,773 galaxies with extinction corrected magnitudes (Schlegel, Finkbeiner & Davis 1998) brighter than $K_s = 11.25$. This magnitude limit corresponds to a median redshift of $z \approx 0.02$ ($\approx 6000 \text{ km s}^{-1}$). Almost all of the 1600 galaxies that remain without redshifts are at very low galactic latitudes ($|b| \lesssim 5^\circ$) or obscured/confused by the dust and the high stellar density towards the Galactic Centre. Figure 1 shows all the objects in 2MRS in Galactic Aitoff Projection. Galaxies with $z \leq 0.01$ are plotted in red, $0.01 < z \leq 0.025$ are plotted in blue, $0.025 < z < 0.05$ are plotted in green and $z \geq 0.05$ are plotted in magenta. Galaxies without measured redshifts are plotted in black. 2MRS can be compared with the deeper 2MASS galaxy catalogue ($K < 14$ th mag) shown in Jarrett (2004, Figure 1).

¹ This is only an approximation. A more realistic model for galaxy clustering is the halo model (e.g. Cooray & Sheth 2002) where the linear bias parameter depends on the mass of the dark matter haloes where the galaxies reside. For this model, the mean number of galaxy pairs in a given halo is usually lower than the Poisson expectation.

² 6dFGS has a much fainter magnitude limit ($K_s = 12.75$) than 2MRS and contains around 150,000 galaxy redshifts. The 6dFGS documentation and the database can be found on the WWW at <http://www.aao.gov.au/local/www/6df/>

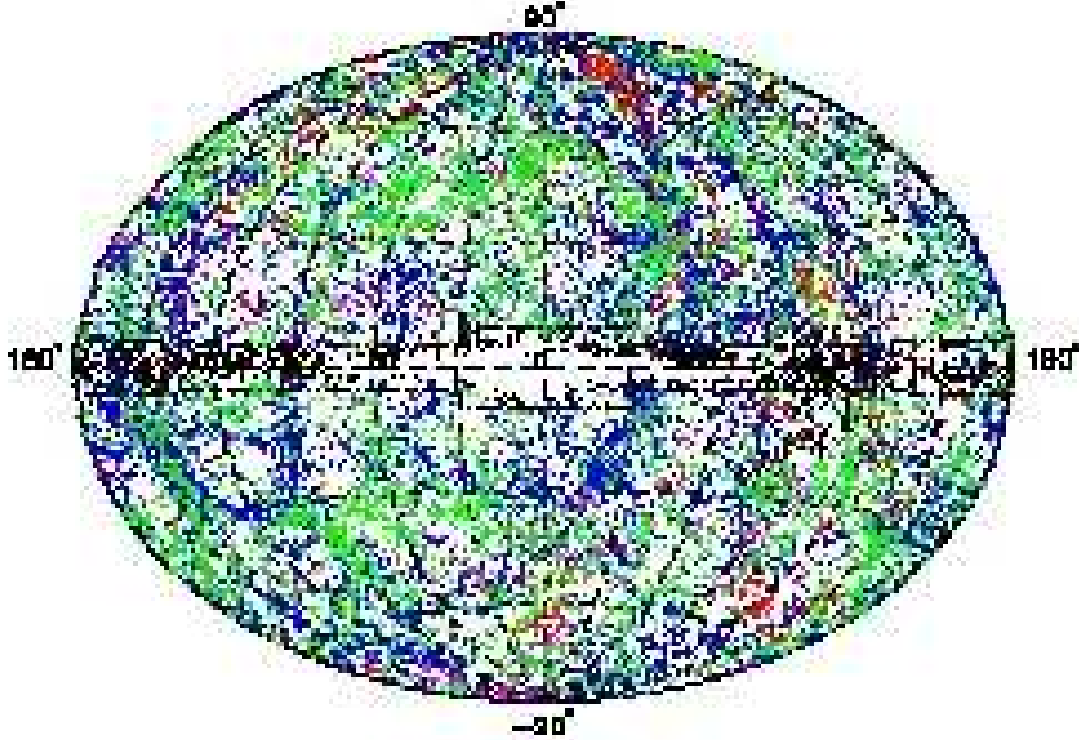


Figure 1. All Objects (24 788 galaxies) in the 2MASS Redshift Catalogue in Galactic Aitoff Projection. The plot contains Galaxies with $z \leq 0.01$ plotted in red, $0.01 < z \leq 0.025$ are plotted in blue, $0.025 < z < 0.05$ are plotted in green and $z \geq 0.05$ are plotted in magenta. Galaxies without measured redshifts are plotted in black. The zone of avoidance is outlined by dashed lines.

2.1 Survey Completeness

2MASS³ has good photometric uniformity and an unprecedented integral sky coverage. The photometric uniformity is better than 4% over the sky including the celestial poles (e.g. Jarrett *et al.* 2000a, 2003) and at magnitudes brighter than $K_s = 12$, 2MASS is essentially complete down to very low galactic latitudes (to b^2o , e.g. Huchra *et al.* 2005). The uniform completeness of the galaxy sample is slightly limited by the presence of foreground stars, for a typical high latitude sky less than 2% of the area is masked. These missing regions are accounted for using a coverage map, defined as the fraction of the area of an $8' \times 8'$ pixel that is not obscured by stars brighter than 10th mag. Galaxies are then weighted by the inverse of the completeness, although the analysis is almost unaffected by this process as the completeness ratio is very close to one for most parts of the sky.

The stellar contamination of the catalogue is low and is reduced further by manually inspecting the objects below a heliocentric redshift of $cz = 200 \text{ km s}^{-1}$. The foreground stellar confusion is highest at low Galactic latitudes, resulting in decreasing overall completeness of the 2MASS catalogue (e.g. Jarrett *et al.* 2000b) and consequently the 2MRS sample. Stellar confusion also produces colour bias in the 2MASS galaxy photometry (Cambresy, Jarrett & Beichman 2005) but this bias should not be significant for 2MRS due to its relatively bright magnitude limit.

2.2 Magnitude and Flux Conversions

2MRS uses the 2MASS magnitude K_{20} , which is defined⁴ as the magnitude inside the circular isophote corresponding to a surface brightness of $\mu_{K_s} = 20 \text{ mag arcsec}^{-2}$ (e.g. Jarrett *et al.* 2000a).

³ 2MASS database and the full documentation are available on the WWW at <http://www.ipac.caltech.edu/2mass>.

⁴ Column 17 (k_m_k20fc) in the 2MASS in the Extended Source Catalogue (XSC)

The isophotal magnitudes underestimate the total luminosity by 10% for the early-type and 20% for the late-type galaxies (Jarrett *et al.* 2003). Following Kochanek *et al.* (2001, Appendix), an offset of $\Delta = -0.20 \pm 0.04$ is added to the K_{20} magnitudes. The galaxy magnitudes are corrected for Galactic extinction using the dust maps of Schlegel, Finkbeiner & Davis (1998) and an extinction correction coefficient of $R_K = 0.35$ (Cardelli, Clayton & Mathis 1989). As expected, the extinction corrections are small for the 2MRS sample. The K_s band k -correction is derived by Kochanek *et al.* (2001) based on the stellar population models of Worthey (1994). The k -correction of $k(z) = -6.0 \log(1+z)$, is independent of galaxy type and valid for $z \lesssim 0.25$.

The flux, S , for each galaxy is computed from the apparent magnitudes using

$$S = S(0 \text{ mag}) 10^{-0.4(K_{20} + ZPO)}, \quad (1)$$

where the zero point offset is $ZPO = 0.017 \pm 0.005$ and $S(0 \text{ mag}) = 1.122 \times 10^{-14} \pm 1.891 \times 10^{-16} \text{ Wcm}^{-2}$ for the K_s band (Cohen, Wheaton & Megeath 2003).

2.3 The Redshift Distribution and the Selection Function

The redshift distribution of 2MRS is shown in Figure 2. The *IRAS* PSCz survey redshift distribution (Saunders *et al.* 2000) is also plotted for comparison. 2MRS samples the galaxy distribution better than the PSCz survey out to $cz = 15000 \text{ km s}^{-1}$. The selection function of the survey (i.e. the probability of detecting a galaxy as a function of distance) is modelled using a parametrised fit to the redshift distribution:

$$dN(z) = Az^\gamma \exp \left[- \left(\frac{z}{z_c} \right)^\alpha \right] dz, \quad (2)$$

with best-fit parameters of $A = 116000 \pm 4000$, $\alpha = 2.108 \pm 0.003$, $\gamma = 1.125 \pm 0.025$ and $z_c = 0.025 \pm 0.001$. This best-fit is also shown in Figure 2 (solid line). The overall selection function $\phi_s(r)$ is the redshift distribution divided by the volume element

$$\phi_s(r) = \frac{1}{\Omega_s r^2} \left(\frac{dN}{dz} \right)_r \left(\frac{dz}{dr} \right)_r \quad (3)$$

where $\Omega_s (\approx 4\pi \text{ steradians})$ is the solid angle of the survey and r is the comoving distance.

3 EXPANSION OF THE DENSITY, VELOCITY AND GRAVITATIONAL POTENTIAL FIELDS IN SPHERICAL HARMONICS

This section describes the spherical harmonic expansion of the density and velocity fields. Spherical harmonics are commonly employed in cosmography of whole-sky surveys for two main reasons. Firstly, separating the observed density field into angular and radial modes concentrates the linear scale redshift distortions into one dimension, making distortions easier to deconvolve. Secondly, both spherical harmonic and Bessel functions are orthogonal and together they form eigenfunctions of the Laplacian operator. These properties lead to very simple relationships between the density, the velocity and the potential fields in harmonic space, allowing the straightforward reconstruction of one field from another observed field. The method used in this paper is based on that developed by FLHLZ. Therefore, we do not give a full description of our method, we only outline the formalism.

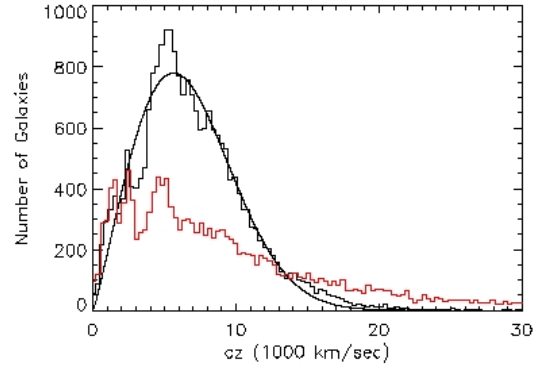


Figure 2. Redshift histogram for 2MRS galaxies and a least squares fit (Equation 2) to the data (black). For comparison, also plotted is a redshift histogram for PSCz galaxies (Saunders *et al.* 2000) (red).

3.1 Expansion of the density field

The density field, $\rho(\mathbf{r})$, can be expanded as a Fourier-Bessel series in the following way:

$$\begin{aligned} \rho(\mathbf{r}) &= \sum_{l=0}^{l_{\max}} \sum_{m=-l}^{+l} \sum_{n=1}^{n_{\max}(l)} C_{ln} \rho_{lmn} j_l(k_n r) Y_{lm}(\theta, \phi) \\ &= \sum_{lmn} C_{ln} \rho_{lmn} j_l(k_n r) Y_{lm}(\theta, \phi). \end{aligned} \quad (4)$$

Here, ρ_{lmn} is the density coefficient, $Y_{lm}(\theta, \phi)$ is the spherical harmonic corresponding to the spherical angular coordinates, $j_l(x)$ is the spherical Bessel function and C_{ln} is the normalisation constant of the spherical Bessel Function. The resolution of the angular modes is determined by the value of l_{\max} and that of the radial modes by the value of $n_{\max}(l)$. In theory, l_{\max} and $n_{\max}(l)$ tend to infinity. In practice, since the distances which galaxy surveys probe are finite, l_{\max} and $n_{\max}(l)$ need to be truncated at finite numbers. This truncation is an effective smoothing of the density field and limits the resolution of the structure in the reconstruction such that the structures smaller than the effective resolution of the highest harmonic, $\Delta\theta \sim \pi/l_{\max}$ (cf. Peebles 1980, Section 46) and the highest radial mode, $\Delta r \sim \pi/k_{n_{\max}}$, will be lost. On the other hand, if the expansion is continued to a very high order the resolution of expansion will be higher than the size of the real structure, introducing artifacts into the reconstruction of density field. The choice of l_{\max} and $n_{\max}(l)$ is discussed in Section 6.

The radial modes, k_n , correspond to a given angular mode l and the C_{ln} s are chosen according to the boundary conditions and to ensure the orthogonality of the spherical Bessel functions. It is assumed that the data are only given within a sphere of radius R and that the logarithmic derivative of the gravitational potential is continuous at $r = R$. The corresponding value of C_{ln} is $1 / \left(\frac{R^3}{2} [j_l(k_n R)]^2 \right)$. The derivation of this result is given in FLHLZ, Appendix A.

Given that the data from a flux-limited redshift catalogue are a set of N discrete points with a redshift-space position vector \mathbf{s} and a weighting function $w(s_i)$, the harmonic density coefficients in redshift space can be derived using the inversion formula,

$$\rho_{lmn}^S = \sum_{i=1}^N w(s_i) j_l(k_n s_i) Y_{lm}^*(\theta_i, \phi_i). \quad (5)$$

where the superscripts S and R hereafter denote redshift and real-space, respectively. We give each galaxy the weight $w(s_i) = 1/\phi_s(s_i)$ and $\phi_s(s_i) (\approx \phi_s(r_i))$ is the selection function of galaxy i .

The density fluctuations, $\delta(\mathbf{s}) = (\rho(\mathbf{s})/\bar{\rho}) - 1$, can be estimated in terms of the Fourier-Bessel function

$$\delta_{lmn}^S = \frac{\rho_{lmn}^S}{\bar{\rho}} - \mathbf{M}_{lmn}, \quad (6)$$

where $\bar{\rho}$ is the mean density of the survey and the second term \mathbf{M}_{lmn} represents a monopole correction (cf. FLHLZ, Equation D14).

3.2 Expansion of the velocity field

The linear theory velocity field in spherical harmonics is given by Regös & Szalay (1989). It is derived by expanding the gravitational potential $\phi(\mathbf{r})$ and the density fluctuations $\delta(\mathbf{r})$ in Fourier-Bessel series, and substituting these into Poisson's equation. Since $j_l(k_n r) Y_{lm}(\theta, \phi)$ is an eigenfunction of the Laplacian operator,

$$\nabla^2 [j_l(k_n r) Y_{lm}(\theta, \phi)] = -k_n^2 j_l(k_n r) Y_{lm}(\theta, \phi), \quad (7)$$

the harmonics of the gravity field can be related to those of the galaxy density field as:

$$\phi_{lmn} = -\frac{3}{2} \Omega_m^{0.6} H_0^2 \frac{\delta_{lmn}^R}{k_n^2}. \quad (8)$$

The radial component of the velocity field, $\mathbf{v}_{\parallel}(\mathbf{r}) = \hat{\mathbf{r}} \cdot \mathbf{v}(\mathbf{r})$, can be decomposed into harmonics as in Equation 4. The harmonic coefficients v_{lmn} for the predicted radial velocity field within $r < R$ are derived by comparing the harmonic expansions of the velocity field and the gravitational potential field:

$$v_{lmn} = \beta H_0 \sum_{n'} (\Xi_l)_{nn'} (\delta_{lmn'}^R), \quad (9)$$

with Ξ as the velocity matrix (cf. FLHLZ, Equation 22).

In spherical harmonics, the LG velocity, $\mathbf{v}(\mathbf{0})$, is written as (see FLHLZ, Appendix C1):

$$\begin{aligned} \mathbf{v}(\mathbf{0}) &= \frac{\beta H_0}{3\sqrt{4\pi}} \sum_{n=1}^{n_{\max}^{(l)}} C_{1n} \int_0^R dr' j_l(k_n r') \\ &\times \left(-\sqrt{2} \operatorname{Re}[\delta_{11n}^R] \mathbf{i} + \sqrt{2} \operatorname{Im}[\delta_{11n}^R] \mathbf{j} + \operatorname{Re}[\delta_{10n}^R] \mathbf{k} \right) \end{aligned} \quad (10)$$

where $\Re[a]$ and $\Im[a]$ refer to the real and imaginary parts of a complex number, a , and R is the radius out to which the density field is measured for the calculation of the velocity.

The harmonics of the transverse velocity field ($\mathbf{v}_{\perp} = -\mathbf{r} \times [\mathbf{r} \times \mathbf{v}(\mathbf{r})]$) are also related to those of the density field. They can be derived using quantum mechanical methods (see FLHLZ, Appendix C2).

4 DECONVOLVING REDSHIFT-SPACE DISTORTIONS IN SPHERICAL HARMONICS

The galaxy peculiar velocities will only introduce distortions in the radial direction, leaving the angular parts intact. Thus, if the density field in redshift-space is expressed in terms of the orthogonal radial and the angular components, as it is the case in the Fourier-Bessel

space, the redshift distortions will only couple the radial modes of the real space density field. This coupling is described by a coupling matrix, $(\mathbf{Z}_l)_{nn'}$ (Fisher *et al.* 1994 and FLHLZ):

$$\delta_{lmn}^S = \sum_{n'=1}^{n_{\max}^{(l)}} (\mathbf{Z}_l)_{nn'} \delta_{lmn'}^R, \quad (11)$$

where $(\mathbf{Z}_l)_{nn'}$ depends only on H_0 , β , $w(r)$ and $\phi_s(r)$ and is independent of the power spectrum⁵. The full derivation of the coupling matrix is given in FLHLZ, Appendix D. We note that Equation 11 is calculated for linear scales only. On small scales, the peculiar velocities introduce radially extended distortions called *Fingers of God*. These distortions can be corrected for either by collapsing the fingers to a point at high density regions or by assuming a Maxwellian distribution for the peculiar velocities (Peacock & Dodds 1994) and deconvolving this distribution from the reconstructed fields (Heavens & Taylor 1995; Erdoğdu *et al.* 2004). In any case, they will not change the constructed fields substantially as they are smoothed out due to the resolution of the spherical harmonics (see Erdoğdu *et al.* 2004 who use who a similar resolution).

In the absence of shot-noise, the real-space density harmonics can simply be obtained by inverting the coupling matrix in Equation 11. However, in the presence of shot-noise, a straight inversion becomes unstable leading to inaccurate estimation of the real-space harmonics. This problem can be overcome by Wiener filtering.

5 WIENER RECONSTRUCTION

In this section, we give the formulae for the Wiener filter method. For a full derivation, we refer the reader to Zaroubi *et al.* (1995) and Erdoğdu *et al.* (2004).

5.1 Model Signal and Noise Matrices

For this analysis, the Wiener-filter reconstructed real-space density field is given by:

$$(\delta_{lmn}^R)_{\text{WF}} = \sum_{n'n''} (\mathbf{S}_l [\mathbf{S}_l + \mathbf{N}_l]^{-1})_{nn'} (\mathbf{Z}_l^{-1})_{n'n''} \delta_{lmn''}^S. \quad (12)$$

For the case $w(r) = 1/\phi_s(r)$, the signal and noise matrices simplify to

$$(\mathbf{S}_l)_{nn'} \simeq P(k_n) C_{ln}^{-1} \delta_{nn'}^K \text{ and} \quad (13)$$

$$(\mathbf{N}_l)_{nn'} = \frac{1}{\bar{\rho}} \int_0^R dr r^2 \frac{1}{\phi_s(r)} j_l(k_n r) j_l(k_{n'} r), \quad (14)$$

respectively.

The expected scatter in the reconstructed density, $\langle \Delta \delta(\mathbf{r}) \rangle^2$ is given by

$$\begin{aligned} \langle \Delta \delta(\mathbf{r}) \rangle^2 &= \frac{1}{4\pi} \sum_{l, n, n'} (2l+1) [(\mathbf{I} - \mathbf{F}_l) \mathbf{S}_l]_{nn'} \\ &\times C_{ln} C_{ln'} j_l(k_n r) j_l(k_{n'} r). \end{aligned} \quad (15)$$

The scatter in the reconstructed radial velocity $\langle \Delta \mathbf{v}_r(\mathbf{r}) \rangle^2$ fields can also be formulated in Fourier-Bessel space in an analogous way

⁵ The coupling matrix has a more complicated dependence on l and m for catalogues with incomplete sky coverage. Zaroubi & Hoffman (1996) derived a similar expression for the coupling matrix in Cartesian coordinates.

(cf. FLHLZ, Appendix F):

$$\begin{aligned} \langle \Delta \mathbf{v}_r(\mathbf{r}) \rangle^2 &= \frac{H_0 \beta^2}{4\pi} \sum_{l n n'} (2l+1) [(\mathbf{I} - \mathbf{F}_l) \mathbf{S}_l]_{nn'} \\ &\times C_{ln} C_{ln'} \frac{j'_l(k_n r) j'_l(k_{n'} r)}{k_n k_{n'}}. \end{aligned} \quad (16)$$

5.2 Choice of Reference Frame

The redshift distortion matrix given in Section 4 takes into account the motion of the observer, $\mathbf{v}(\mathbf{0})$, and thus the choice of reference frame is arbitrary. On the other hand, the formulation of $(\mathbf{Z}_l)_{nn'}$ involves the Taylor expansion of the velocity field out to first order in $\Delta \mathbf{v} = \mathbf{v}(\mathbf{r}) - \mathbf{v}(\mathbf{0})$ (see Appendix D of FLHLZ). As such, the reconstruction will be more accurate in the frame in which $\Delta \mathbf{v}$ is smaller. Nearby where the galaxies share the LG motion, it is more accurate to correct for the redshift distortions in the LG frame. At larger distances, galaxy motions are independent of the LG velocity and thus $\Delta \mathbf{v}$ is smaller in the CMB frame. Since 2MRS probes the local universe ($cz_{\text{med}} \approx 6000 \text{ km s}^{-1}$), we will work with the LG frame redshifts. We will present the dipole velocity results from redshifts in both frames.

The choice of frame for the redshifts will not affect the frame of the reconstructed density field. In both cases, the reconstructed harmonics will be in real-space. Consequently, the reconstructed velocity field (Equation 9) will be in the CMB frame. It is possible to convert the velocity field into the LG frame by subtracting the Local Group velocity ($v_{LG} = 627 \pm 22 \text{ km s}^{-1}$, towards $l_{LG} = 273^\circ \pm 3^\circ$, $b_{LG} = 29^\circ \pm 3^\circ$, Bennett *et al.* 2003 and Courteau & Van Den Bergh 1999). In the following section, the reconstructed velocity maps will be presented in either the LG or the CMB frames. Up to 8000 km s^{-1} (Figures 11, 12, 13 and 14) it is difficult to see the real nature of the structures in the LG frame as the LG velocity dominates. Therefore, the maps will be plotted in the CMB frame. On larger distances (Figures 15, 16, 17 and 18), galaxies have positive CMB radial velocities so it is easier to compare the velocities in the LG frame than in the CMB frame.

6 APPLICATION TO THE TWO MASS REDSHIFT SURVEY

The formalism discussed in the previous sections is limited to 4π sky coverage. In principle, the analysis can be extended to account explicitly for incomplete sky coverage. In this paper, a simpler approach has been adopted to fill in the galaxies masked by the Galactic Plane (the *Zone of Avoidance*). The masked area is divided into 36 bins of 10° in longitude. In each angular bin, the distance is divided into bins of $10 h^{-1} \text{ Mpc}$. The galaxies in each longitude/distance bin are then sampled from the corresponding longitude/distance bins in the adjacent strips $-|b_{\text{masked}}| - 10^\circ < b < |b_{\text{masked}}| + 10^\circ$ (where $|b_{\text{masked}}| = 5^\circ$ or $|b_{\text{masked}}| = 10^\circ$). These galaxies are then placed in random latitudes within the mask region. The number of galaxies in each masked bin is set to a random Poisson deviate whose mean equals the mean number of galaxies in the adjacent unmasked strips. This procedure is carried out to mimic the shot noise effects. The success of this interpolation method depends on the interplay between the width of the mask, the angular resolution and whether the structure in the adjacent regions physically correlate with the structure in the Zone of Avoidance. The method is less robust for masked areas larger than $|b| = 15^\circ$ (Lahav *et al.* 1994). The width of the 2MRS mask is much smaller than

this value and the survey penetrates deep into the Zone of Avoidance apart from very obscured regions near the centre of the Milky Way. We also test the effects of our method by varying the bin sizes and by filling the region uniformly instead of interpolating. We calculate the angular power-spectrum for each case and find good agreement (Rassat *et al.* 2006) between them.

The density field is expanded within a spherical volume of radius $R_{\text{max}} = 20000 \text{ km s}^{-1}$. We impose the condition that the density field outside R_{max} is zero and the logarithmic derivative of the gravitational potential is continuous at the boundary (which holds if $j_{l-1}(k_n R) = 0$ for all l). There are two other possible boundary conditions discussed in FLHLZ: setting only the density or the radial velocity zero at the boundary. We have tested our reconstructions using these boundary conditions. Setting the density to zero at the boundary results in a discontinuous potential and the reconstructed radial velocities become unrealistically high. Up to a distance of 10000 km s^{-1} , the fields reconstructed using the zero velocity boundary condition agree reasonably well with those reconstructed using the continuous potential condition, however the radial velocities of the zero velocity reconstructions are slightly higher. Beyond 10000 km s^{-1} , the radial velocities of the zero velocity reconstructions tend to zero, however the backside infall into the Shapley Supercluster still exists. Thus we conclude that setting the logarithmic derivative of the gravitational potential to be continuous at the boundary allows for a *smooth* transition of the density and velocity fields from $r < R_{\text{max}}$ to $r > R_{\text{max}}$ and as such gives the most robust results. We also note that FLHLZ, WLF and Schmoldt *et al.* (1999) use the same boundary condition for their reconstructions.

The resolution of the reconstruction depends on the maximum values of angular and radial modes (see Figure 6 of WLF). We want to have as high a resolution as possible without introducing artificial structures to the field. Therefore, we compute the harmonics up to $l_{\text{max}} = 15$ angularly and $k_n R \leq 100$ radially. $l_{\text{max}} = 15$ is chosen so that the angular resolution ($\delta\theta \sim \pi/l$) is comparable to the width of the interpolated region and the radial modes are chosen to match the angular resolution (see FLHLZ, Appendix B for a detailed discussion).

The Wiener filter method requires a model for the linear galaxy power spectrum in redshift-space, which depends on the real-space power spectrum and on the redshift distortion parameter, $\beta \equiv \Omega_m^{0.6}/b$. The real-space power spectrum is well described by a scale-invariant Cold Dark Matter power spectrum with shape parameter $\Gamma \approx \Omega_m h$, for the scales concerned in this analysis. The combined analysis of third year data from the Wilkinson Microwave Anisotropy Probe (WMAP, Spergel *et al.* 2006), the Two Degree Field Galaxy Redshift Survey (2dFGRS, Cole *et al.* 2005) and the Sloan Digital Sky Survey (Tegmark *et al.* 2004) imply $\Gamma \approx 0.17$. On the other hand Frith, Outram & Shanks (2005) and Maller *et al.* (2005) analyse the angular power spectrum of the 2MASS galaxies and derive lower Γ values of 0.14 ± 0.02 and 0.116 ± 0.009 , respectively. The normalisation of the power spectrum is conventionally expressed in terms of the variance of the mass density field in spheres of $8h^{-1} \text{ Mpc}$, σ_8 . Recent WMAP results combined with the 2dFGRS gives $\sigma_8 \approx 0.75$, whereas analysis of the 2MASS galaxies suggest $\sigma_8 \approx 0.9$ (Frith, Outram & Shanks 2005, Maller *et al.* 2005, Pike & Hudson 2005). In a previous paper, we analysed the 2MRS LG dipole and derived a value for β for 2MRS: $\beta = 0.4 \pm 0.09$ (Erdoğdu *et al.* 2006).

In order to check the goodness of fit of these different parameters to the data, we calculate the χ^2 statistic defined by

$$\chi^2 = \mathbf{d}^\dagger (\mathbf{S} + \mathbf{N})^{-1} \mathbf{d}, \quad (17)$$

for $\Gamma = (0.1, 0.2)$, $\sigma_8 = (0.7, 0.9)$ and $\beta = (0.3, 0.4, 0.5)$. Changing Γ does not affect the χ^2 values greatly but $\Gamma = 0.2$ is a slightly better fit. Varying σ_8 is a bit more influential on the χ^2 values, however, the reconstructed maps look very similar for these models. Increasing Γ decreases the power on large scales and, therefore, the peculiar velocities tend to be smaller but the difference is negligible. Decreasing σ_8 has the same effect on the power spectrum as increasing Γ . The choice of β plays a more important role in the goodness-of-fit results but has little effect on the reconstructed maps other than a linear scaling of peculiar velocities. In the analysis that follows, we adopt $\Gamma = 0.2$, $\sigma_8 = 0.7$ and $\beta = 0.5$, which is the best fit model that was considered, with a reduced χ^2 value of 1.3. We note that the best fit β is higher than derived in Erdoğan *et al.* (2006), this discrepancy will be discussed in Section 6.3. In a forthcoming paper (Rassat *et al.* 2006), we will present a detailed analysis of the cosmological parameters of 2MRS.

6.1 Density Maps

Figures 3, 4, 5, 6, 7, 8, 9 and 10 show the Aitoff projections of the reconstructed density field in real-space, plotted in Galactic coordinates, evaluated at different distance slices.

Figure 3 shows a thin density shell at $r = 2000 \text{ km s}^{-1}$. The expected scatter in the reconstructed density field is $\langle \Delta\delta(\mathbf{r}) \rangle = 0.31$ and this value stays approximately the same out to $r = 10000 \text{ km s}^{-1}$ and increases by 0.1 thereafter. All the known structures are resolved and the field at this distance is dominated by inter-connecting voids. The Puppis cluster (Lahav *et al.* 1993, S1 in Saunders *et al.* 1991) is very prominent and extends down to $b \simeq -28^\circ$. The overdensity labelled as C1 ($l \simeq 190^\circ$, $b \simeq 5^\circ$) does not correspond to any previously observed structure.

Figure 4 is the 2MRS density field at $r = 4000 \text{ km s}^{-1}$. Hydra ($l \simeq 270^\circ$, $b \simeq 50^\circ$) and Centaurus ($l \simeq 300^\circ$, $b \simeq 20^\circ$) continue in this shell but now are separated by the Hydra void. Centaurus is connected to the new overdensities C2 ($l \simeq 345^\circ$, $b \simeq 10^\circ$) and C8 ($l \simeq 295^\circ$, $b \simeq 7^\circ$) and Hydra connects to C4 ($l \simeq 240^\circ$, $b \simeq 25^\circ$). Pavo-Indus-Telescopium continues deep into the Zone of Avoidance and connects to the Centaurus Wall as suggested by Fairall (1988). The well-known cluster Cancer ($l \simeq 210^\circ$, $b \simeq 30^\circ$), as well as new clusters C3 ($l \simeq 275^\circ$, $b \simeq -30^\circ$), C5 ($l \simeq 195^\circ$, $b \simeq 0^\circ$), C6 ($l \simeq 170^\circ$, $b \simeq -15^\circ$) and C7 ($l \simeq 55^\circ$, $b \simeq 15^\circ$), all peak at $r = 5000 \text{ km s}^{-1}$ with C5, C6 and C7 connecting to Pegasus and the Perseus-Pisces Wall. The overdensity C ϵ (WLF) is more prominent in the 2MRS field than in *IRAS* 1.2 Jy field. The Perseus and Pisces clusters are picked up as two distinct overdensities and both connect to Camelopardalis ($l \simeq 145^\circ$, $b \simeq 30^\circ$) and Cetus ($l \simeq 190^\circ$, $b \simeq -55^\circ$) at $r = 5000 \text{ km s}^{-1}$.

Figure 5 is the density field at $r = 6000 \text{ km s}^{-1}$. Hydra ($l \simeq 285^\circ$, $b \simeq 5^\circ$) is less prominent in this shell whereas Pavo-Indus-Telescopium ($l \simeq 0^\circ$, $b \simeq -45^\circ$) is still strong. The cluster Abell 3627 (or Norma, $l \simeq 330^\circ$, $b \simeq -10^\circ$) which was recognised as the centre of the Great Attractor⁶ by Kraan-Korteweg *et al.* (1996), peaks around $r = 5000 \text{ km s}^{-1}$ and is separated from the Centaurus Wall by the Sculptor Void. The overdensity labelled

as C8 continues from the previous shell and contains the luminous CIZA J1324.7-5736, cluster which was discovered by Ebeling, Mullis & Tully (2002) and the Centaurus-Crux cluster (Woudt, 1998). The Abell clusters 569 ($l \simeq 155^\circ$, $b \simeq -15^\circ$) and 168 ($l \simeq 120^\circ$, $b \simeq 70^\circ$) are as prominent as the Perseus-Pisces ridge and both are connected to it. The clusters labelled as WLB (e.g. WLB 248 at $l \simeq 240^\circ$, $b \simeq 40^\circ$) were identified by White *et al.* (1999). There are two previously unidentified voids at this distance labelled as V1 and V2 and a cluster at ($l \simeq 240^\circ$, $b \simeq 8^\circ$) labelled C9.

Figure 6 is the 2MRS density field at $r = 8000 \text{ km s}^{-1}$. The Great Wall (Geller & Huchra 1989) connects to the Ophiuchus supercluster discovered by Wakamatsu *et al.* (1994). The massive Shapley supercluster is already visible ($l \simeq 300^\circ$, $b \simeq 30^\circ$) at this distance. The void V1 continues to this shell. The new clusters C10 ($l \simeq 205^\circ$, $b \simeq 10^\circ$), C11 ($l \simeq 250^\circ$, $b \simeq -10^\circ$), C12 ($l \simeq 325^\circ$, $b \simeq -10^\circ$) and C13 ($l \simeq 85^\circ$, $b \simeq 13^\circ$) lie on galactic latitudes. The cluster ZwCl 0943.7+5454 was first identified by Zwicky & Herzog (1966) and K42 by Klemola (1969). All the superclusters labelled as SC (e.g. SC 129 in this shell) are given in Einasto *et al.* (1997, Table 2) and structures labelled CAN and CID (e.g. CAN 136 in this shell and CID 15 in the next shell) are clusters given in Wegner *et al.* (1999).

Figure 7 is the 2MRS density field at $r = 10000 \text{ km s}^{-1}$. The expected scatter now rises to $\langle \Delta\delta(\mathbf{r}) \rangle = 0.36$. The mighty Hercules supercluster dominates this shell and Shapley begins to appear. Other dominant structures are CID (CAN) 15 & 16.

Figure 8 is the 2MRS density field at $r = 12000 \text{ km s}^{-1}$ and has a scatter of $\langle \Delta\delta(\mathbf{r}) \rangle = 0.41$. The Perseus-Pegasus and Pisces (Einasto *et al.* 1997) superclusters, C20 and Abell 576 continue the Perseus-Pisces wall and dominate the shell.

Figure 9 is the 2MRS density field at $r = 14000 \text{ km s}^{-1}$ with scatter $\langle \Delta\delta(\mathbf{r}) \rangle = 0.46$. The density field of the Shapley supercluster peaks at this distance and connects to C28 and C29 at $r = 15000 \text{ km s}^{-1}$ to form a ridge.

Figure 10 is the 2MRS density field at $r = 16000 \text{ km s}^{-1}$. The expected scatter is $\langle \Delta\delta(\mathbf{r}) \rangle = 0.49$. The most conspicuous structure is the Pisces-Cetus supercluster, which connects to the Southern Great Wall. The Perseus-Cetus also dominates the southern strips of the 2dF (see e.g. Erdoğan *et al.* 2004, Porter & Raychaudhury 2005) and Sloan surveys (e.g. Porter & Raychaudhury 2005). We note that at this distance, we do not pick up any voids. This is due to the nature of our technique. The Wiener filter method will predict the mean field in the absence of data. Since the density field is constructed to have zero mean, the Wiener filter signal will approach to zero at the edges of the survey where the shot noise dominates. This leads to the signal being reconstructed in a non-uniform manner. As such, we do not present maps of the density and velocity fields beyond 16000 km s^{-1} after which the shot noise is too high and the Wiener Filtered fields tend to zero.

6.2 Velocity Maps

Figures 11, 12, 13, 14, 15, 16, 17 and 18 show the Galactic Aitoff projections of the radial velocity fields for $\beta = 0.5$ evaluated across the same shells as the density fields shown in Figures 3, 4, 5, 6, 7, 8, 9 and 10. Positive (outflowing) radial velocities are shown as solid lines and the negative (infalling) radial velocities are shown as dashed lines. The contour spacing is $|\Delta v_{\text{radial}}| = 50 \text{ km s}^{-1}$.

Figures 11 & 12 show the CMB frame radial velocity fields at $r = 2000 \text{ km s}^{-1}$ and at $r = 4000 \text{ km s}^{-1}$, respectively. The ex-

⁶ By ‘Great Attractor’, it is meant the entire steradian on the sky centred at ($l \sim 310^\circ$, $b \sim 20^\circ$) covering a distance of $20 h^{-1} \text{ Mpc}$ to $60 h^{-1} \text{ Mpc}$.

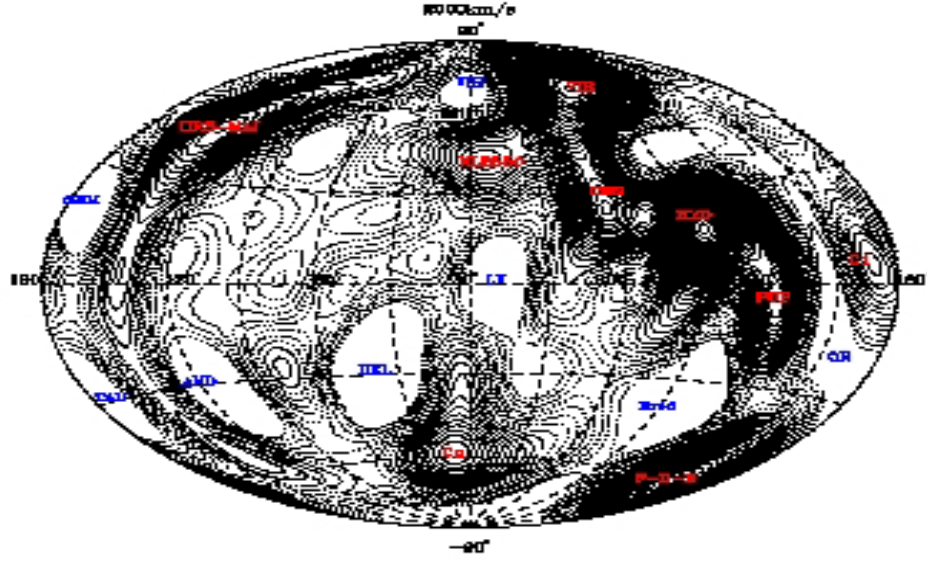


Figure 3. The reconstructed density field, evaluated on a thin shell at 2000 km s^{-1} , shown in Galactic Aitoff projection. Dashed lines show $\delta < 0$, and solid lines show $\delta \geq 0$, with contour spacing $|\Delta\delta| = 0.1$. The overdense regions are (from left to right) Ursa Major (Urs-Maj), WLB 550, C α , Virgo (Vir), Centaurus (Cen), Hydra (Hyd), Puppis (Pup), Fornax-Doradus-Eridanus (F-D-E) and C1. The voids are Gemini (Gem), Taurus (Tau), Andromeda (And), Delphinus (Del), Virgo (Vir), Local Void (LV), Eridanus (Erid) and Orion (Or).

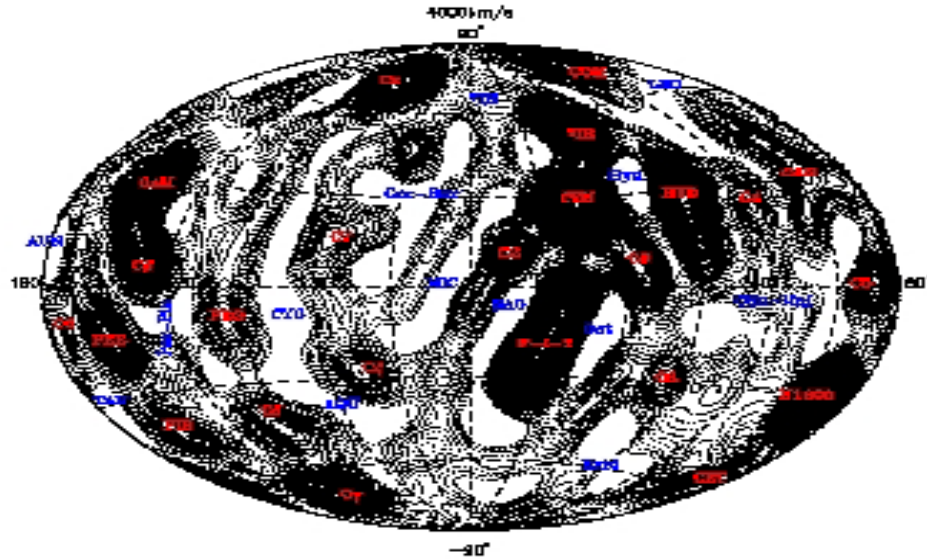


Figure 4. Same as Figure 3 but evaluated at 4000 km s^{-1} . The overdense regions are C6, Perseus (Per), Pisces (Pis), Camelopardalis (Cam), C β , Pegasus (Peg), C δ , C γ , C ϵ , C7, C ζ , C2, Coma (Com), Virgo (Vir), Centaurus (Cen), Pavo-Indus-Telescopium (P-I-T), C8, Hydra (Hyd), C3, C4, Cancer (Can), NGC 1600 (N1600), Cetus (Cet) and C5. The voids are Aunga (Aun), Taurus (Tau), Perseus-Pisces (Per-Pis), Cygnus (Cyg), Aquarius (Aqu), Corona Borealis (Cor-Bor), Microscopium (Mic), Virgo (Vir), Sagittarius (Sag), Hydra (Hyd), Octans (Oct), Leo, Eridanus (Erid) and Canis Major (Can-Maj).

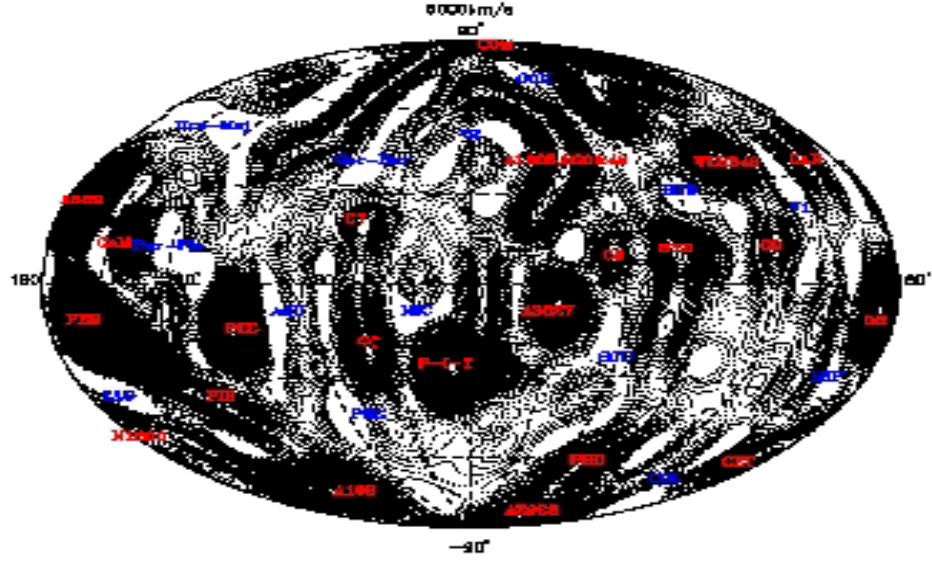


Figure 5. Same as in Figure 3 but evaluated at 6000 km s^{-1} . The overdensities are Abell 569 (A569), Perseus (Per), Pisces (Pis), NGC 1600 (N1600), Abell 168, Camelopardalis (Cam), Pegasus (Peg), C7, C ζ , Pavo-Indus-Telescopium (P-I-T), Abell Clusters 1605, 300 & 42, Abell 3627, C8, Phoenix (Pho), Abell 2923, Coma (Com), Hydra (Hyd), WLB 248, C9, Cancer (Can), Orion (Or) and Cetus (Cet). The voids are Taurus (Tau), Ursa Major (Urs-Maj), Perseus-Pisces (Per-Pis), Aquarius (Aqu), Corona-Borealis (Cor-Bor), Pegasus (Peg), V2, Microscopium (Mic), Coma (Com), Sculptor (Scu), Columba (Col), V1 and Lepus (Lep).

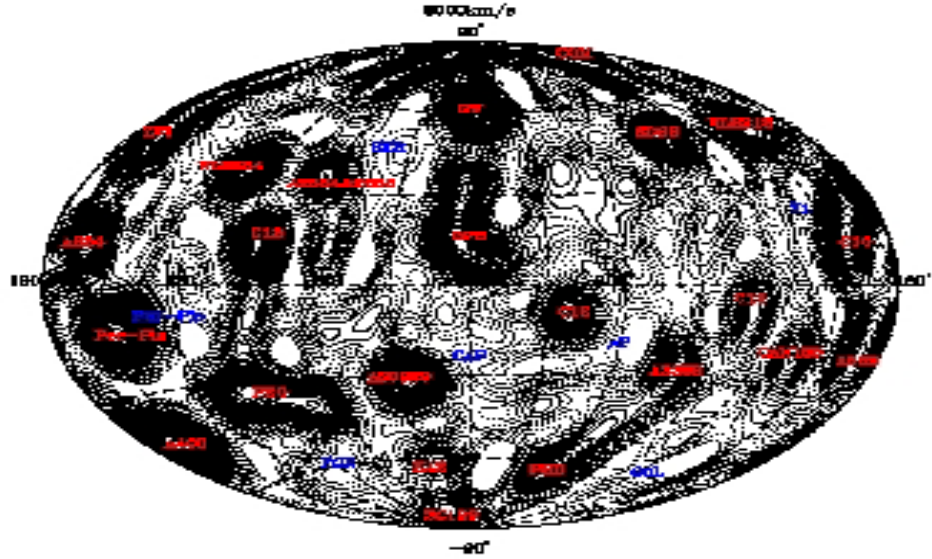


Figure 6. Same as in Figure 3 but evaluated at 8000 km s^{-1} . The overdensities are ZwCl 0943.7+5454 (ZWI), Abell 634, Perseus-Pisces (Per-Pis), Abell 400, WLB 664, C13, Pegasus (Peg), Abell Clusters 2634 & 2666, Abell S0929, Klemola 42 (K42), Great Wall (GW), Ophiuchus (Oph), SC 129, C12, Phoenix (Pho), Coma (Com), SDSS CE J159.778641-00.784376 (SDSS), Abell 3389, WLB 213, C11, CAN 136, C10 and Abell 539. The voids are Perseus-Pisces (Per-Pis), Fornax (For), Serpens (Ser), Capricornus (Cap), Apus (Ap), Columba (Col) and V1.

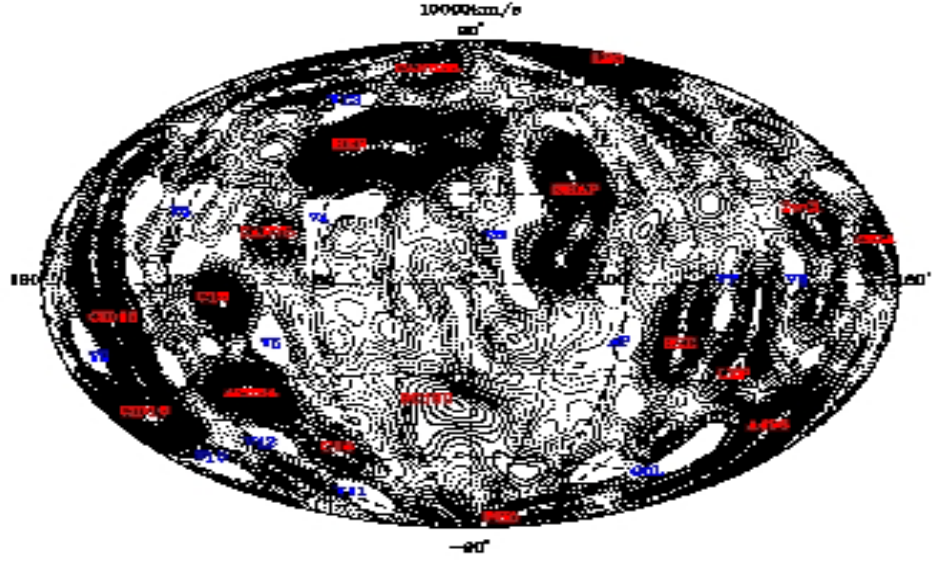


Figure 7. Same as in Figure 3 but evaluated at 10000 km s^{-1} . The overdensities are CID 15, CID16, C13, Abell 2634, C14, CAN 75, CAN 338, Hercules (Her), SC180, Shapley (Shap), Phoenix (Pho), Leo, RXC J0712.0-6030, Lepus (Lep), ZwCl 0820.6+0436, Abell 496 and CIZA J0603.8+2939. The voids are V9, V6, V10, V12, V11, V13, V5, V4, V3, Apus (Ap), V7, Columba (Col) and V8.

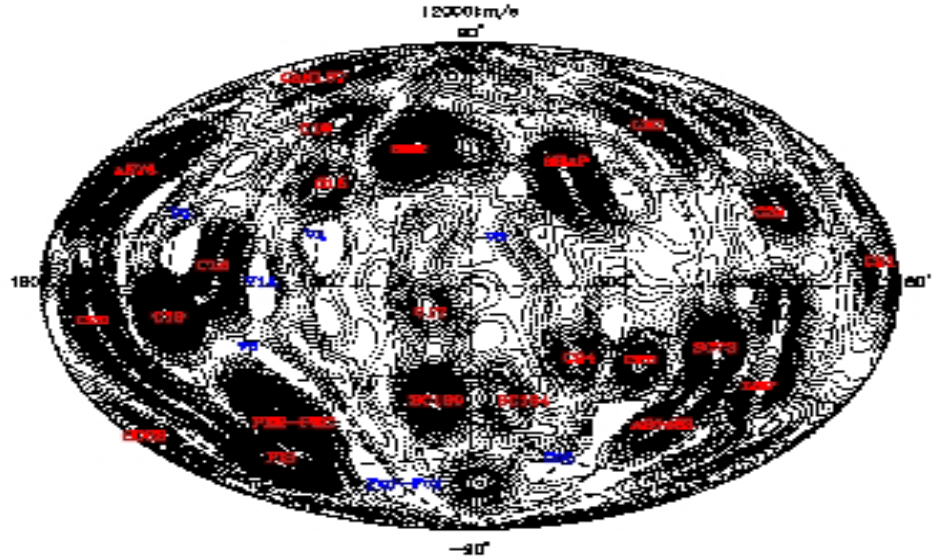


Figure 8. Same as in Figure 3 but evaluated at 12000 km s^{-1} . The overdensities are SDSS clusters SDSS CE J048.551922-00.613762 and SDSS CE J050.935932-00.117944 (SDSS), Abell 576, C20, Pisces (Pis), CAN 137, C19, C18, Perseus-Pegasus (Per-Peg), C16, C15, Hercules (Her), C17, SC180, SC194, Shapley (Shap), C24, C23, Leo, SC73, Abell S0463, C22, Lepus (Lep) and C21. The voids are V6, V14, V5, V4, Further-Fornax (Fur-For), V3 and Columba (Col).

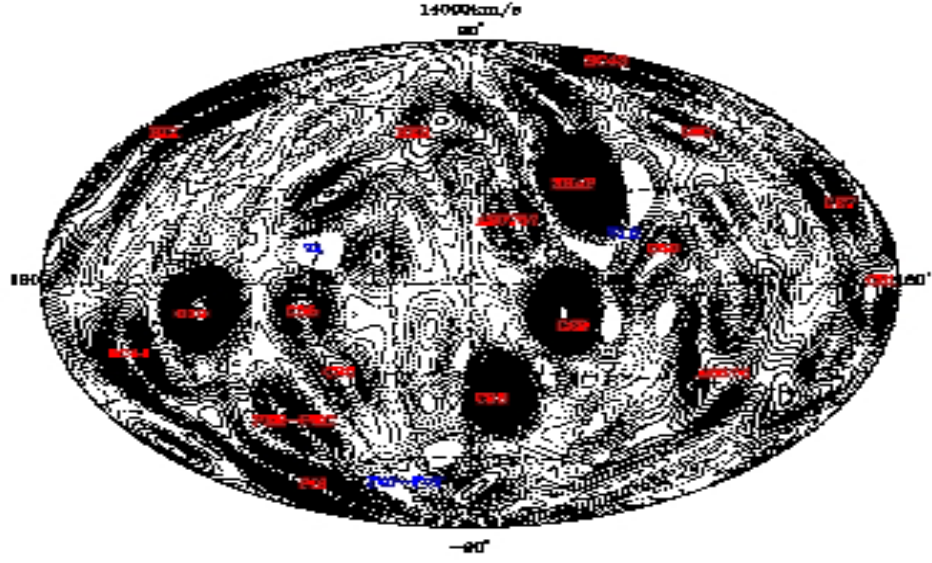


Figure 9. Same as in Figure 3 but evaluated at 14000 km s^{-1} . The overdensities are Rixos F231.526 (RIX), SC44, C19, Pisces (Pis), Perseus-Pegasus (Per-Peg), C25, C26, Hercules (Her), Abell S0757, C28, Shapley (Shap), C29, C30, SC 43, Leo, Abell 3376, C27 and C21. The voids are V4, Further-Fornax (Fur-For) and V15.

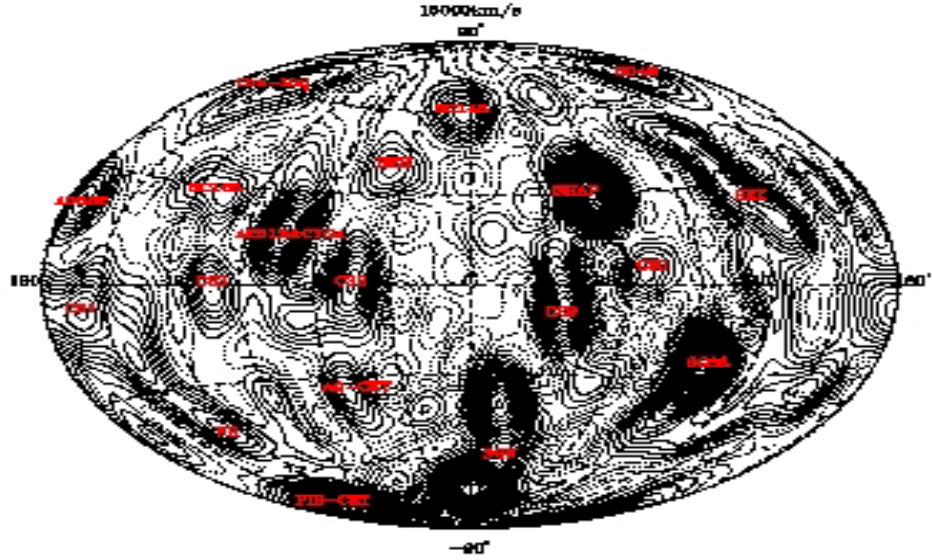


Figure 10. Same as in Figure 3 but evaluated at 16000 km s^{-1} . The overdensities are Abell 582, C31, Ursa-Major (Urs-Maj), SC168, West 9 (W9), C33, Abell 2319 & Cygnus A (CYGA), Pisces-Cetus (Pis-Cet), C32, Aquarius-Cetus (Aq-Cet), Hercules (Her), SC143, Southern Great Wall (SGW), C29, Shapley (Shap), C30, SC43, Sextans (Sex) and SC68.

pected scatter in the velocity field is $\langle \Delta \mathbf{v}(\mathbf{r}) \rangle = 53 \text{ km s}^{-1}$ at $r = 2000 \text{ km s}^{-1}$ and $\langle \Delta \mathbf{v}(\mathbf{r}) \rangle = 62 \text{ km s}^{-1}$ at $r = 4000 \text{ km s}^{-1}$. At $r = 2000 \text{ km s}^{-1}$, there is a strong outflow towards the Virgo-Great Attractor ($l \simeq 290^\circ$, $b \simeq 15^\circ$) and inflow out of the underdense regions. Also seen at this distances are the effects of Perseus-Pisces and N1600, causing a strong outflow towards ($l \simeq 165^\circ$, $b \simeq -30^\circ$). At $r = 4000 \text{ km s}^{-1}$, Perseus-Pisces and N1600 are the dominant structures causing an outflow towards ($l \simeq 150^\circ$, $b \simeq -20^\circ$). There is also a flow towards the centre of Pavo-Indus-Telescopium ($l \simeq 335^\circ$, $b \simeq -25^\circ$) and a back-side infall to Hydra. The back-side infall to the Great Attractor region becomes strongest at $r = 5000 \text{ km s}^{-1}$ and reaches to $v_{\text{infall}} = (982 \pm 400) \text{ km s}^{-1}$ in the Local Group frame and $v_{\text{infall}} = (127 \pm 409) \text{ km s}^{-1}$ in the CMB frame, where the quoted values are the mean of the velocity field around the region and the error bars are the standard deviation from that mean and the expected scatter in the velocity field added in quadrature.

Although still visible at $r = 4000 \text{ km s}^{-1}$, the Great Wall really starts to dominate in **Figure 13** at a distance of $r = 6000 \text{ km s}^{-1}$. At this distance the velocity scatter rises to $\langle \Delta \mathbf{v}(\mathbf{r}) \rangle = 72 \text{ km s}^{-1}$. Here the fall towards the Coma Cluster is quite apparent at $l \simeq 240^\circ$ and $b \simeq 80^\circ$. The velocity flow towards Perseus-Pisces is still strong and there is some outflow towards Pegasus ($l \simeq 95^\circ$, $b \simeq -60^\circ$), Phoenix ($l \simeq 330^\circ$, $b \simeq -75^\circ$), the Abell clusters A548, A539 ($l \simeq 230^\circ$, $b \simeq -20^\circ$) and A400 ($l \simeq 175^\circ$, $b \simeq -45^\circ$). The CMB radial velocities at $r = 8000 \text{ km s}^{-1}$, shown in **Figure 14**, have scatter of $\langle \Delta \mathbf{v}(\mathbf{r}) \rangle = 87 \text{ km s}^{-1}$ and are mostly outflowing apart from the remnants of back-side infall towards the Great Attractor and the Coma cluster. By $r = 10000 \text{ km s}^{-1}$, it becomes difficult to compare peculiar velocities in the CMB frame so we switch to the LG frame. At $r = 10000 \text{ km s}^{-1}$ (**Figure 15**, $\langle \Delta \mathbf{v}(\mathbf{r}) \rangle = 108 \text{ km s}^{-1}$), the dipole velocity of the LG is still visible, however there is an outflow towards Shapley ($l \simeq 310^\circ$, $b \simeq 25^\circ$) and the Hercules supercluster ($l \simeq 20^\circ$, $b \simeq 45^\circ$). Shapley outflow becomes stronger at $r = 12000 \text{ km s}^{-1}$ (**Figure 16**, $\langle \Delta \mathbf{v}(\mathbf{r}) \rangle = 130 \text{ km s}^{-1}$), begins to decrease at $r = 14000 \text{ km s}^{-1}$ (**Figure 17**, $\langle \Delta \mathbf{v}(\mathbf{r}) \rangle = 146 \text{ km s}^{-1}$) and at $r = 16000 \text{ km s}^{-1}$ (**Figure 18**, $\langle \Delta \mathbf{v}(\mathbf{r}) \rangle = 150 \text{ km s}^{-1}$) there is a strong back-side infall towards it.

Figure 19 shows the 2MRS density and velocity fields in the Supergalactic plane ($SGZ = 0 \text{ km s}^{-1}$) in different reference frames. The top plot is the reconstructed three-dimensional peculiar velocity field in the CMB frame, superimposed on the reconstructed density field in the Supergalactic plane. The bottom plot is the same as the one on the left but the superimposed peculiar velocity field is reconstructed in the LG frame (obtained by subtracting the Local Group velocity ($v_{LG} = 627 \pm 22 \text{ km s}^{-1}$, towards $l_{LG} = 273^\circ \pm 3^\circ$, $b_{LG} = 29^\circ \pm 3^\circ$). The extent of the planar density distribution in the Supergalactic plane can clearly be seen in these plots. Since the Local Group is moving towards the Great Attractor/Shapley region, the strong outflow towards the positive y-plane seen in the top plot decreases in the bottom plot. For the same reason, the outflow towards the negative y-plane is much stronger in the LG frame (bottom plot) than in the CMB frame. The most intriguing result is the connectivity of the Shapley supercluster ($SGX, SGY = (-12000, 7000)$) to the Great Attractor region. The Virgo cluster at ($SGX, SGY = (0, 1000)$) also appears connected to the Great Attractor. The Perseus-Pisces supercluster also is visible at ($SGX, SGY = (2500, -4500)$) and Camelopardalis is at ($SGX, SGY = (45, -30)$). The other visible superclusters are Columba at ($SGX, SGY = (7500, -11000)$) and Hercules ($SGX, SGY = (-13000, -4000)$). In both plots, the outflow is

dominated by Shapley, particularly in the CMB frame. The flow towards Virgo and the Perseus-Pisces region is also apparent and the flow towards the Great Attractor is clearly visible. Also observed is a significant flow towards Columba and some towards Hercules. After 16000 km s^{-1} , the shot noise is too high and the density field becomes non-uniform.

Over the past years, there has been some disagreement over the existence of back-side infall towards the GA (e.g. Dressler & Faber 1990 and Mathewson *et al.* 1992). We find a clear back-side infall, visible in both plots and in particular the one in the LG frame. The highest velocity back-falling velocity around the GA region is $800 \pm 600 \text{ km s}^{-1}$ (at $55h^{-1} \text{ Mpc}$) in the CMB frame. In **Figure 20**, we plot the average radial velocity field in towards the centres of the GA ($290^\circ \leq l \leq 320^\circ$, $-25^\circ \leq b \leq 60^\circ - 25^\circ \leq b \leq 70^\circ$, $r \leq 80h^{-1} \text{ Mpc}$) and the Shapley ($290^\circ \leq l \leq 320^\circ$, $40^\circ \leq b \leq 70^\circ$, $r \geq 80h^{-1} \text{ Mpc}$) Superclusters as a function of distance. The red lines are for the LG frame and the black lines are for the CMB frame. The solid lines denote the mean of the reconstructed velocities and the dashed lines are the errors calculated from the standard deviation of velocities in that region and the expected velocity scatter added in quadrature. In this plot, the back infall onto the GA and the subsequent outflow towards Shapley are clearly visible. An observer in the GA would see the surrounding nearby galaxies moving towards her. On larger scales, she would observe a dipole velocity towards Shapley. If she was in the Shapley Supercluster (at $r \approx 130h^{-1} \text{ Mpc}$), she would observe that the surrounding galaxies are moving towards her. Whilst, this back-side infall onto the GA was also observed by FLHLZ, WLF and Schmoldt *et al.* (1999), other authors who applied different reconstruction techniques to *IRAS* galaxy catalogues (e.g. Davis, Nusser & Willick 1996; Branchini *et al.* 1999; Valentine, Saunders and Taylor 2000) find little evidence of it. Although the 2MRS sample is the densest all-sky sample to date and as such allows the most precise reconstruction of the local velocity field, our results are still not conclusive. In a forthcoming paper we will compare the reconstructed fields with the observed velocity fields based on the distance measurements to elliptical galaxies in the 6dFGS and a new survey of spirals in the I Band (SFI++) to assess the significance of this back-side infall.

6.3 Alternative Reconstruction Methods

In order to assess the effects of the systematic errors of our method, we also carried out the reconstructions using alternative methods. **Figure 21** shows several of these reconstructions on the Supergalactic Plane (SGP) out to 6000 km s^{-1} . The top left plot is the unsmoothed harmonic reconstruction of the 2MRS density field in redshift space. It can clearly be seen that the harmonics are strongly affected by shot noise. Overdensities follow circular paths about the origin as a result of correlations introduced by noise. These artifacts are still clearly evident in the top right plot where the density field is corrected for redshift distortions (using Equation 11) but without noise suppression. The correction of the redshift distortions reduces the overall amplitude of the density contrasts and makes the structures more spherical. This reconstruction corresponds to the unbiased minimal variance (umv) estimation of Zaroubi (2002) since in our case the redshift distortion matrix is invertible. The bottom left panel shows the real space density field after the Wiener Filter has been applied. As expected the Wiener Filter mitigates the effects of shot noise, removing the artifacts and high frequency harmonics from the map, however, the Wiener reconstructed field is biased towards the mean field which is zero by

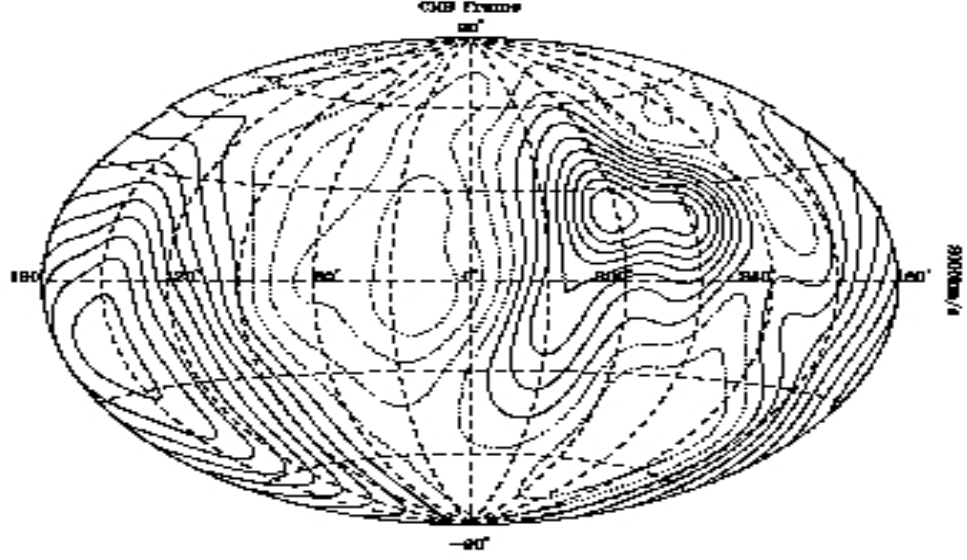


Figure 11. The reconstructed radial velocity field, evaluated on a thin shell at 2000 km s^{-1} , shown in Galactic Aitoff projection in the CMB frame. This velocity field corresponds with the density field shown in Figure 3. Dashed lines show inflow, and solid lines show outflow. The first solid line is for $v_{\text{radial}} = 0 \text{ km s}^{-1}$, and contour spacing is $|\Delta v_{\text{radial}}| = 50 \text{ km s}^{-1}$. Note the strong outflow towards the Great Attractor and flow out of the Local Void. Also Perseus-Pisces and N1600, cause an outflow towards ($l \simeq 165^\circ$, $b \simeq -30^\circ$)

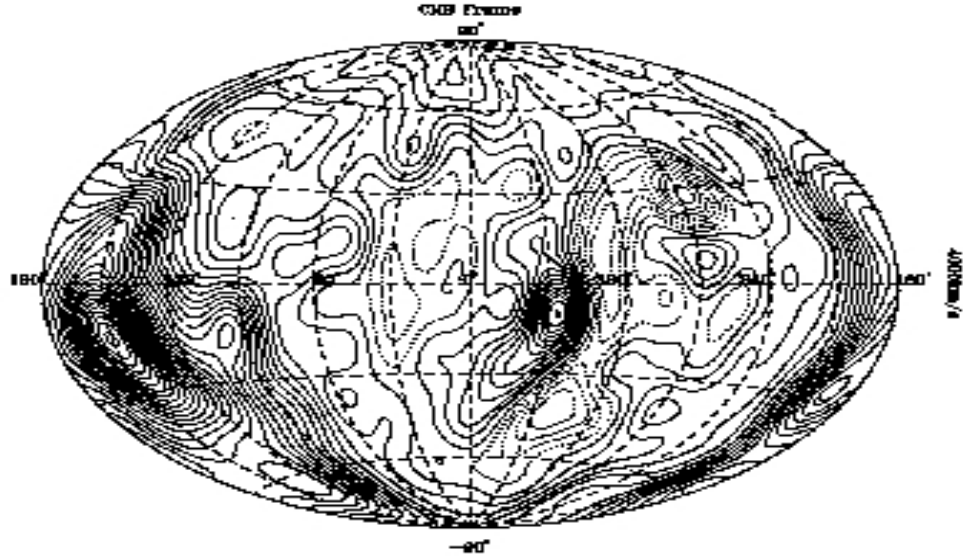


Figure 12. Same as Figure 11 but evaluated at 4000 km s^{-1} . This velocity field corresponds with the density field shown in Figure 4. Note Perseus-Pisces and N1600 cause the strongest outflow towards ($l \simeq 150^\circ$, $b \simeq -20^\circ$). There is also a flow towards the centre of Pavo-Indus-Telescopium ($l \simeq 335^\circ$, $b \simeq -25^\circ$) and a weaker one towards Hydra ($l \simeq 280^\circ$, $b \simeq 10^\circ$).

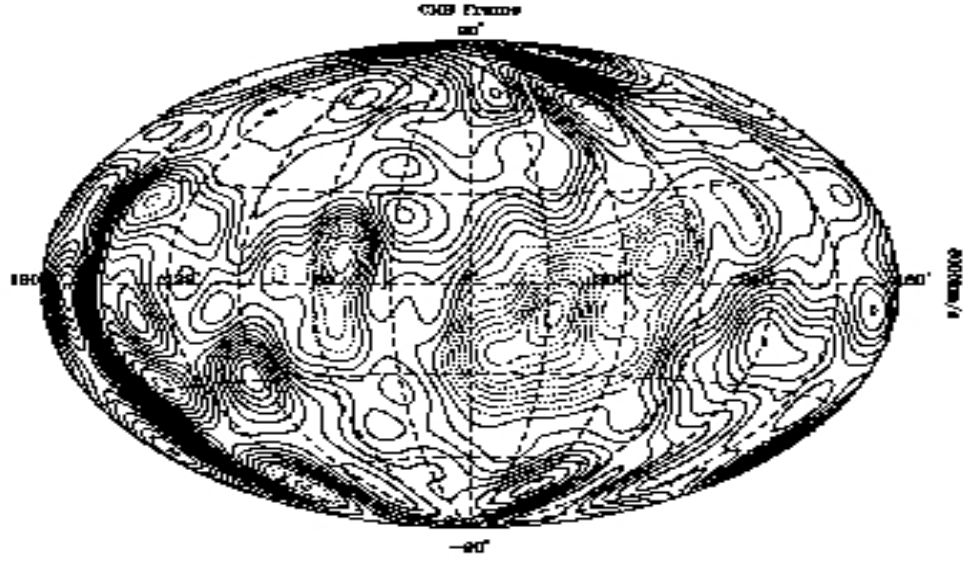


Figure 13. Same as Figure 11 but evaluated at 6000 km s^{-1} . This velocity field corresponds with the density field shown in Figure 5. Note the strong outflow towards the Great Wall, especially towards Coma and the general velocity flow towards the North Galactic Pole from the South Galactic Pole. There is still some outflow towards Pegasus. Also visible is a strong back-side infall towards the Great Attractor region and Perseus-Pisces.

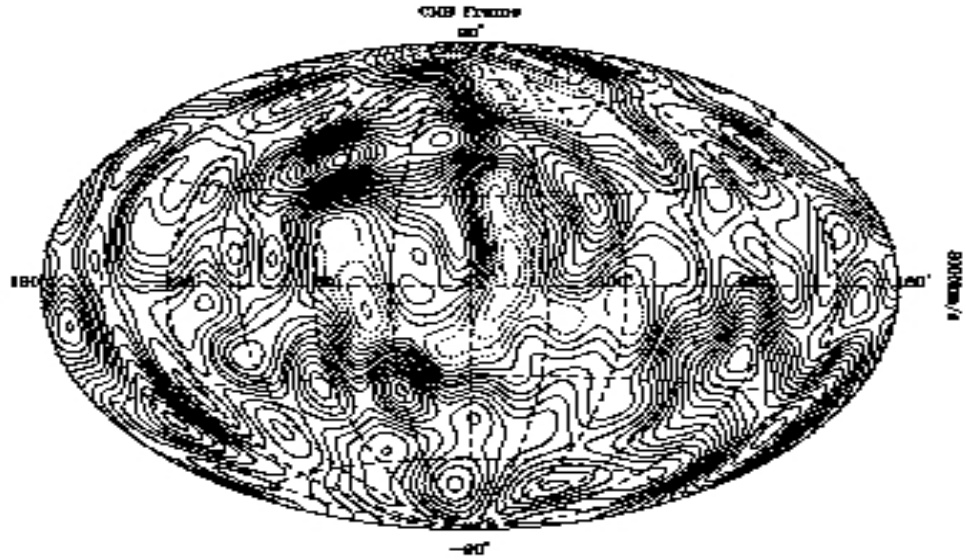


Figure 14. Same as Figure 11 but evaluated at 8000 km s^{-1} . This velocity field corresponds with the density field shown in Figure 5. There is still a strong outflow towards the clusters of the Great Wall. The outflow towards Shapley ($l \simeq 310^\circ$, $b \simeq 25^\circ$) is already visible. The Sculptor Wall is implied in the outflow towards the Southern Galactic Pole.

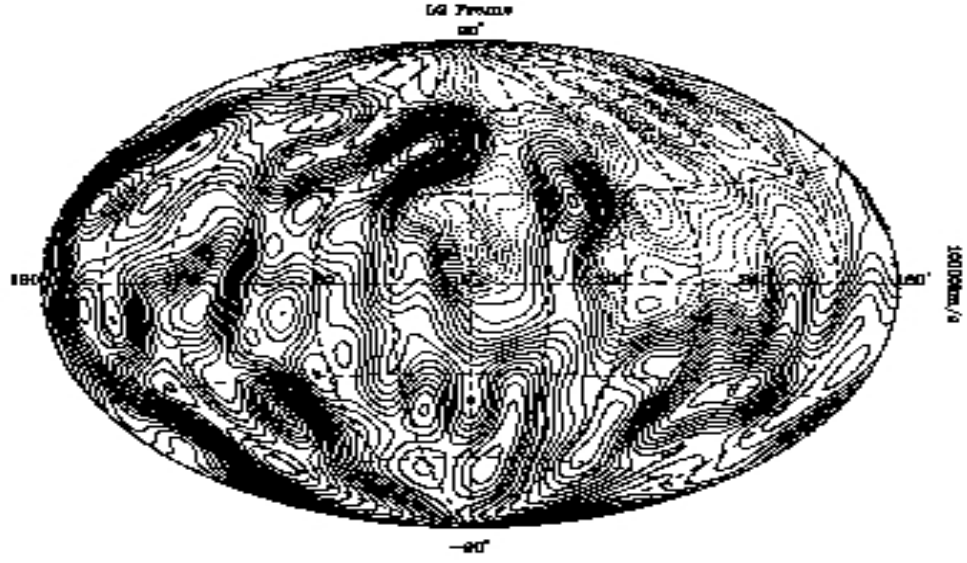


Figure 15. Same as Figure 11 but evaluated at 10000 km s^{-1} and in the LG Frame instead of the CMB Frame. There are three superclusters that dominate the outflow, Hercules towards ($l \simeq 20^\circ$, $b \simeq 45^\circ$), Shapley towards ($l \simeq 320^\circ$, $b \simeq 25^\circ$) and Columba towards ($l \simeq 225^\circ$, $b \simeq -30^\circ$).

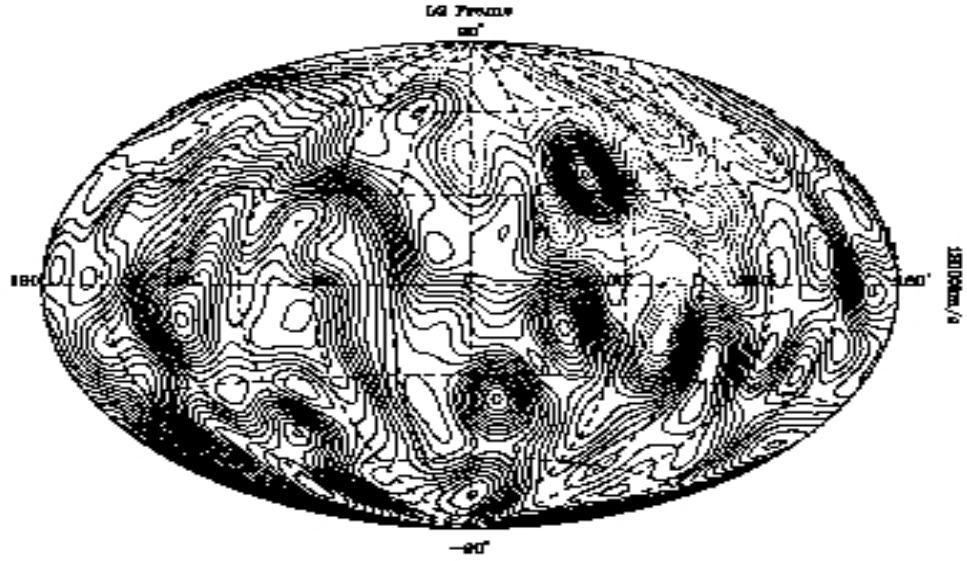


Figure 16. Same as Figure 11 but evaluated at 12000 km s^{-1} and in the LG Frame instead of the CMB Frame.

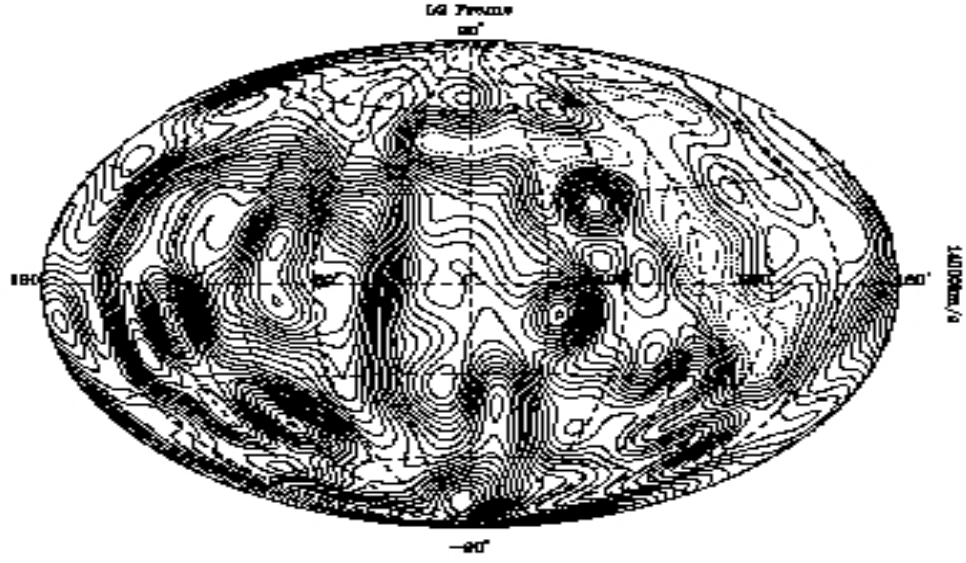


Figure 17. Same as Figure 11 but evaluated at 14000 km s^{-1} and in the LG Frame instead of the CMB Frame.

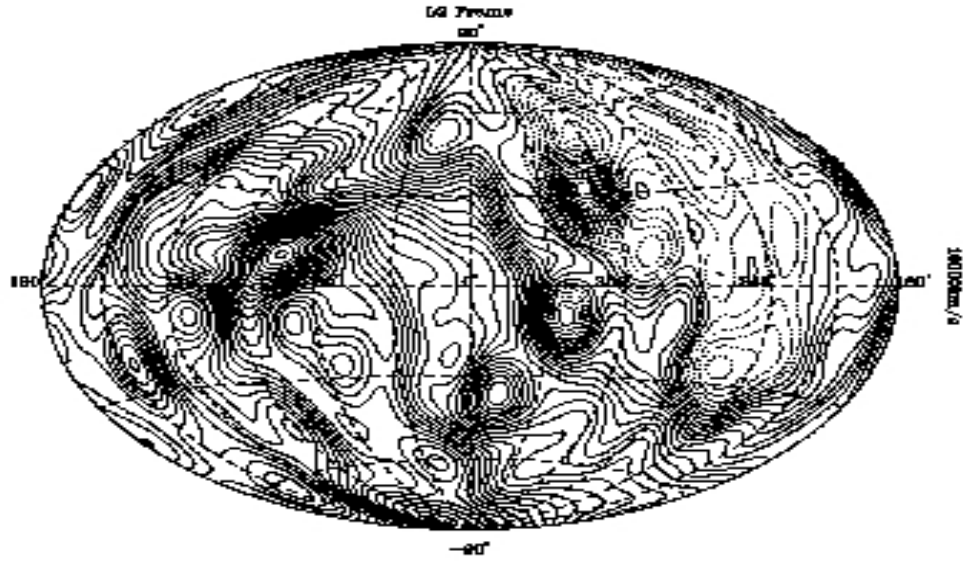


Figure 18. Same as Figure 11 but evaluated at 16000 km s^{-1} and in the LG Frame instead of the CMB Frame.

construction. In fact, the variance of the Wiener Filtered field is always smaller than the variance of the *true* underlying field. In order to overcome this drawback, Yahil (1994) introduced an alternative filter which preserves the power in the underlying field. This filter is defined as the square root of the Wiener Filter. With this defini-

tion, the filtered field equals to that of the true field. The bottom right panel shows the real-space density field reconstructed using Yahil's filter. Whilst the estimated field is unbiased, the reconstruction is not optimal in the sense of minimum variance and there are artifacts due to insufficient reduction of noise.

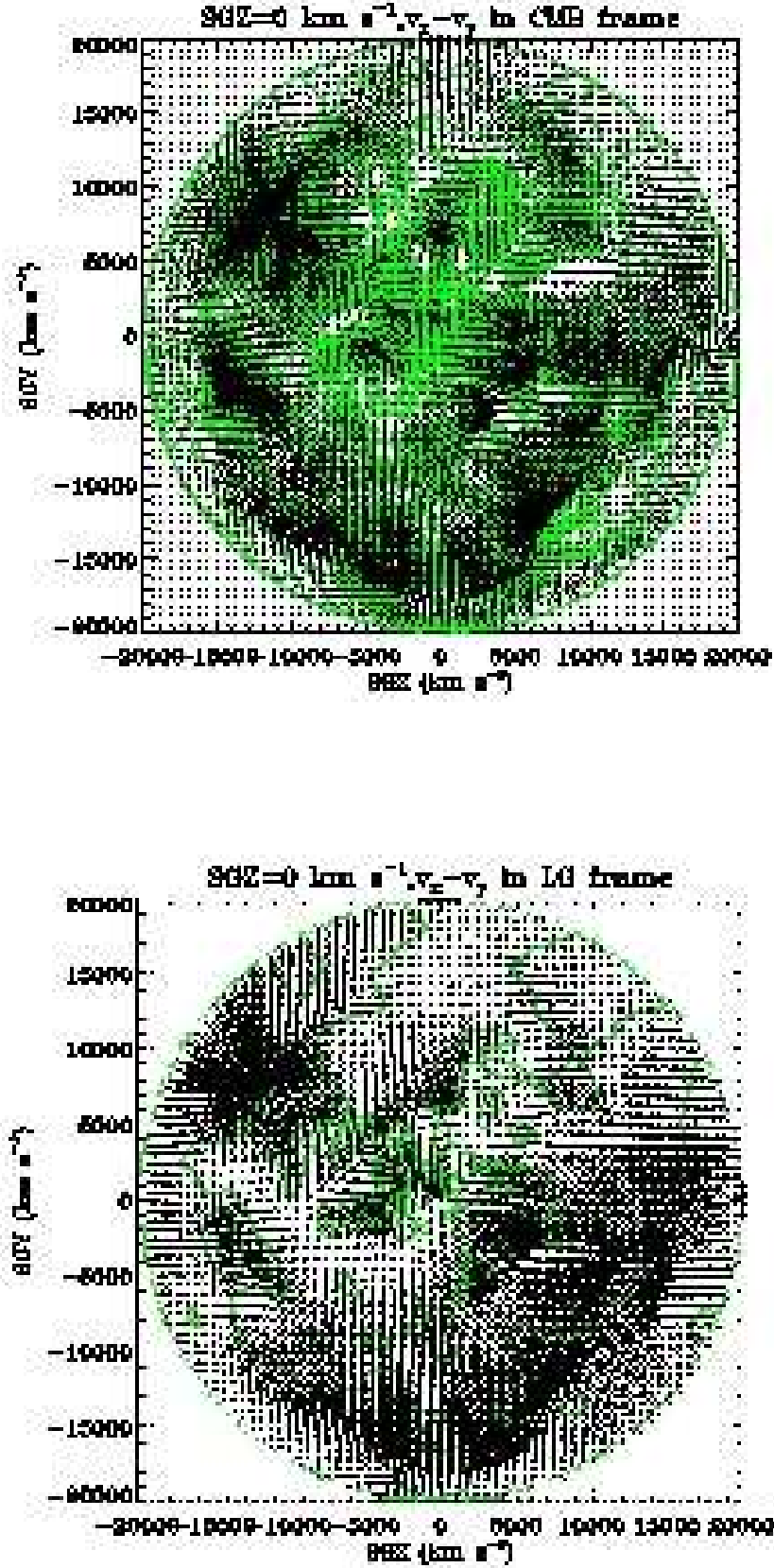


Figure 19. The reconstructed density fields in the supergalactic plane. The spacing of the density contours is $|\Delta\delta| = 0.1$ with dashed lines denoting the negative and the solid line denoting the positive density contrast. Superimposed in black are the reconstructed three-dimensional peculiar velocity field in the CMB (top plot) and the LG (bottom plot) frames. The length of the arrows are about 300 km s^{-1} per cell. The main overdensities are Hydra-Centaurus

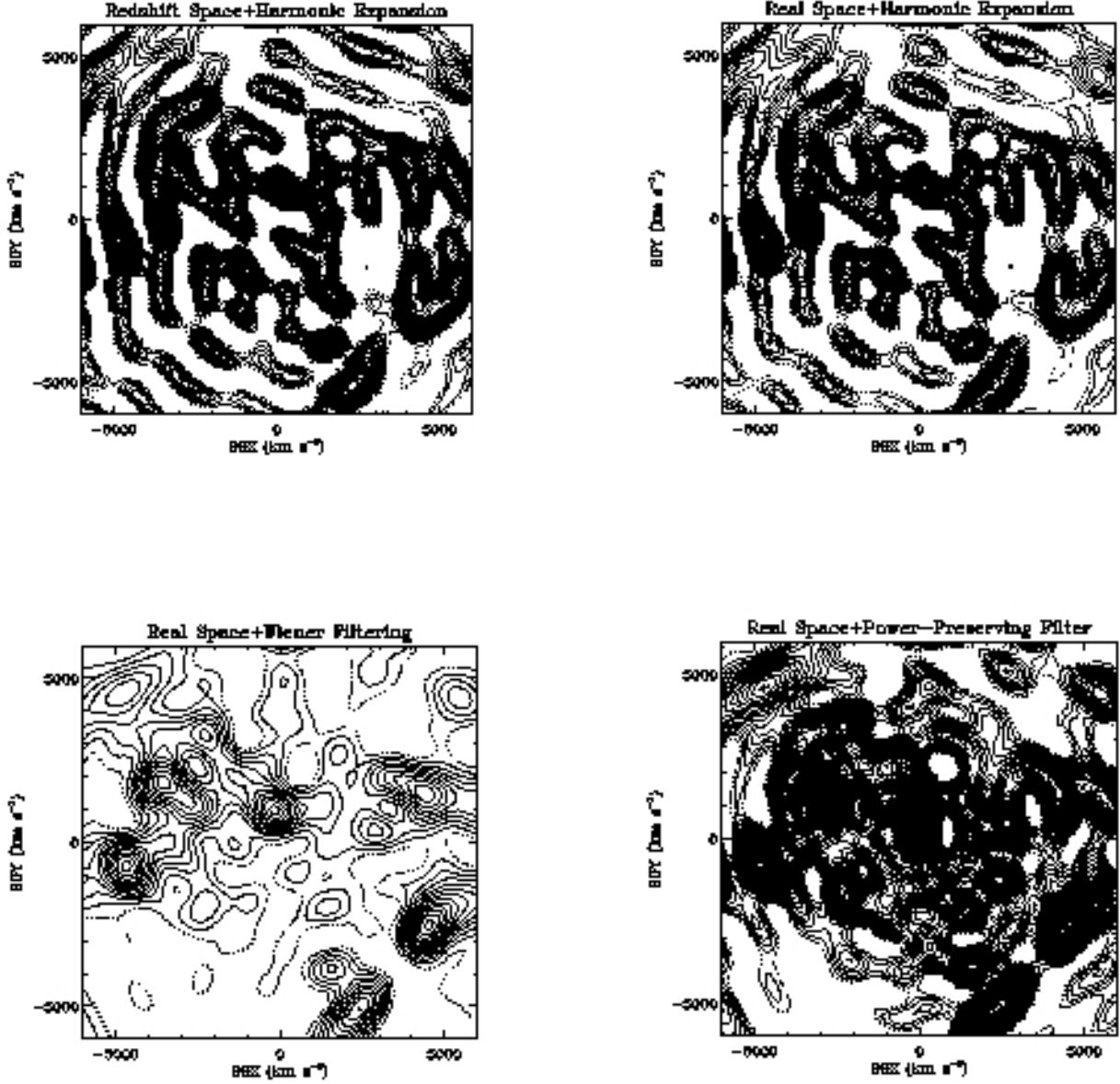


Figure 21. Reconstructions of the 2MRS density field in the Supergalactic Plane. All contours are spaced at $|\Delta\delta| = 0.5$, with solid (dashed) contours denoting positive (negative) contours. Top left: The density field expanded in spherical harmonics with no smoothing. Top right: Same as in top left but with the harmonics corrected for redshift distortion. Bottom left: Same as in top right but smoothed by the Wiener Filter. Bottom Right: The real space density field smoothed by the power preserving filter.

6.4 The acceleration of the Local Group

A detailed calculation of the acceleration of LG using the 2MRS data was given by Erdoğdu *et al.* (2006). In this section, the LG velocity is reconstructed from the density field. There are two main advantages of the analysis performed in this paper. Firstly, working with spherical harmonic allows for reliable correction of the velocity flows and secondly, the Wiener filtering suppresses the noise self-consistently. The LG dipole is linear in the galaxy density field (assuming linear biasing). Consequently, the dipole computed from

the Wiener filter algorithm will be an optimal (in the sense of minimum variance) estimate of the dipole due to matter within the reconstruction volume as long as non-linear effects can be neglected.

The reconstructed 2MRS dipole (Equation 10) and the expected scatter (Equation 16) in the reconstruction is plotted as a function of distance in the top plot of Figure 22. The bottom plot of Figure 22 shows the angle between the direction of the LG dipole and the CMB dipole ($l = 273^\circ$, $b = 29^\circ$). The black line is the dipole reconstructed with $\beta = 0.5$ (rescaled to $\beta = 1.0$) and the dashed line denotes the scatter in the velocity reconstruction. The

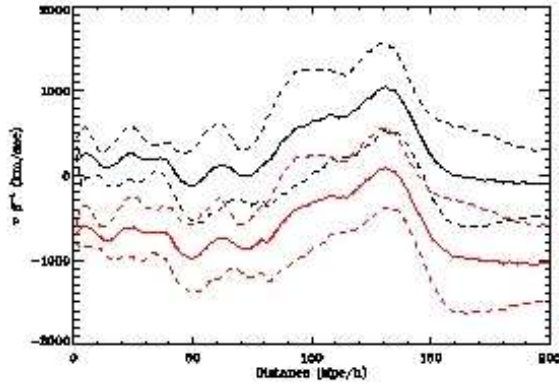


Figure 20. The radial velocity field in the region of the GA and the Shapley Superclusters as a function of distance. The red lines are for the LG and the black lines are for the CMB frame. The solid lines denote the mean of the reconstructed velocities and the dashed lines are the errors calculated from the standard deviation of velocities and the expected velocity scatter added in quadrature. The regions with negative velocities move towards us and positive velocities move away from us.

inversion of the radial coupling matrix introduces a non-linear relationship between the value of β and the amplitude of the reconstructed acceleration. To illustrate this, we also plot the dipole reconstructed with $\beta = 1.0$ (the green line). The amplitudes of the dipole reconstructions using $\beta = 0.5$ and $\beta = 1.0$ are in good agreement (within the expected scatter) and the misalignment angles are almost the same up to 13000 km s^{-1} . The blue line is the dipole reconstructed with $\beta = 0.5$ from the CMB redshifts. As expected, the amplitude of the dipole is underestimated at nearby distances and the misalignment angle is bigger than the dipole reconstructed from the LG redshifts. We conclude that, since the LG dipole is dominated by nearby galaxies, it is more accurate to use the LG redshifts in the reconstruction.

We also plot the number-weighted dipole obtained using raw redshifts (solid red line Erdoğdu *et al.* 2006) and the associated shot noise (dashed red line). The bottom plot indicates that the direction of the Wiener-reconstructed dipole is consistent with the dipole obtained in Erdoğdu *et al.* 2006). Both dipoles show the ‘tug of war’ between the Great Attractor and Perseus-Pisces and the dipole velocities are dominated by structure within the distance of $50 h^{-1} \text{ Mpc}$. However, the amplitude of the Wiener dipole is less than the number-weighted dipole. This is due to the fact that in the previous paper, we did not filter the shot noise errors. Furthermore, in the previous paper, we did not take peculiar velocities into account when calculating the number-weighted dipole and these will lead to the over-estimation of the LG-frame dipole (the *Rocket Effect*). The value for β we obtain by equating the CMB dipole measurements with our reconstructed dipole reflects the decrease in the amplitude. We get $\beta = 0.54 \pm 0.12$ at 13000 km s^{-1} whereas we find $\beta = 0.40 \pm 0.09$ at 13000 km s^{-1} in Erdoğdu *et al.* (2006). The convergence of the direction of the LG dipole does not seem affected by the velocity corrections but there is in general better alignment between the Wiener-reconstructed LG dipole and the CMB dipole than the LG dipole, calculated directly from the raw data and the CMB dipole. The misalignment angle of the Wiener dipole

from the LG redshifts is almost as that of the raw-data dipole up to 13000 km s^{-1} and the angle is 39° at this distance. At least half of this misalignment is probably due to the fact that when we modeled the LG dipole, we assumed all the galaxies have the same weight (see Erdoğdu *et al.* 2006). Also our analysis uses linear perturbation theory which is correct only to first order δ . There may be contributions to the LG dipole from small scales which would cause gravity and the velocity vectors to misalign.

7 SUMMARY AND CONCLUSIONS

In this paper, the Wiener reconstruction technique was applied to recover real-space density and velocity fields from 2MRS. The observed density field was first expanded in terms of spherical harmonics and spherical Bessel functions (Equations 4 and 6) which are both orthogonal and which together satisfy Poisson’s equation. Then, the redshift distortions, described by the coupling matrix \mathbf{Z} , were corrected for by the matrix inversion of \mathbf{Z} in Equation 11, assuming linear theory and a value of $\beta = \Omega^{0.6}/b = 0.5$. After the inversion, the real-space density field was estimated using the Wiener filter for a given CDM power spectrum with $\sigma_8 = 0.7$ and $\Gamma = 0.2$ (Equations 12, 13 and 14). Finally, the velocity field is reconstructed from the Wiener-filtered density field using Equations 9.

The reconstructed density field resolves most of the known structures as well as new clusters and voids. The density and velocity fields agree well with the *IRAS* PSCz and 1.2-Jy fields derived using the Wiener filter technique. There is a back-side infall towards the Great Attractor region, in agreement with Schmoldt *et al.* (1999) and FLHLZ. There is a strong outflow towards the Shapley supercluster which suggests that Shapley plays an important dynamical role in the local velocity field.

The LG dipole derived from the reconstructed velocity field is lower in amplitude at all distances than the LG dipole derived from the raw data by Erdoğdu *et al.* (2006). The misalignment angle between the CMB dipole and the 2MRS dipole decreases down to 13° at 5000 km s^{-1} and its amplitude is about $800 \beta \text{ km s}^{-1}$. If our canonical value for β is correct then this suggests most of the acceleration is generated within 5000 km s^{-1} and the structure at higher distances contributes less than 30% to the LG dipole. The ‘tug-of-war’ between the Great Attractor and the Perseus-Pisces supercluster to which the dipole is commonly attributed can clearly be seen in Figure 11. The 2MRS dipole agrees well with the best-fit value for the canonical model to the data with $\beta = 0.5$, for fixed $\Gamma = 0.2$ and $\sigma_8 = 0.7$.

The Wiener filter technique performs very well and provides a rigorous reconstruction method determined by the data and the expected signal. In a forthcoming paper, we will compare the reconstructed fields with the peculiar velocities from the 6dF survey. This will allow us to test the validity of our reconstructions and enable the refinement of our method.

ACKNOWLEDGEMENTS

Special thanks to Peter Coles, Yehuda Hoffman, Michelle Lanyon, Karen Masters and Chris Short for their valuable comments. PE would like thank the University College London for its hospitality during the completion of this work. OL acknowledges a PPARC Senior Research Fellowship. JPH, LM, CSK, NM, and TJ are supported by NSF grant AST-0406906, and EF’s research is partially

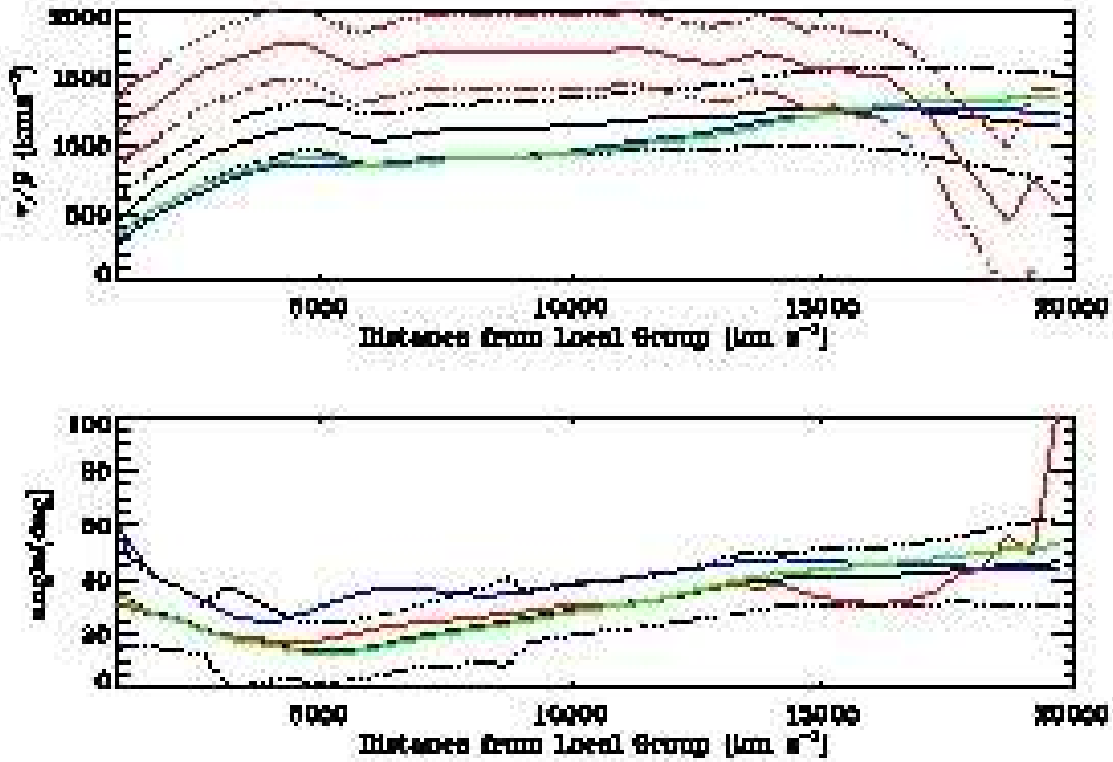


Figure 22. Top Plot: The growth of acceleration of the Local Group due to galaxies within a series of successively larger concentric spheres centred on the local group. The growth of estimated shot noise is also shown as dashed lines. The black line is the dipole reconstructed with $\beta = 0.5$. The blue line is the dipole reconstructed with $\beta = 0.5$ from the CMB redshifts. The green line is the dipole reconstructed with $\beta = 1.0$. The red line is the dipole from Erdoğdu *et al.* (2006) and the dashed line is the associated shot noise. Bottom: The angle between the CMB dipole ($l = 273^\circ$, $b = 29^\circ$) and the reconstructed Local Group velocity. The lines are colour coded to coincide with the top plot. The dashed lines denote the shot noise errors.

supported by the Smithsonian Institution. DHJ is supported as a Research Associate by Australian Research Council Discovery-Projects Grant (DP-0208876), administered by the Australian National University. This publication makes use of data products from the Two Micron All Sky Survey, which is a joint project of the University of Massachusetts and the Infrared Processing and Analysis Center/California Institute of Technology, funded by the National Aeronautics and Space Administration and the National Science Foundation. This research has also made use of the NASA/IPAC Extragalactic Database (NED) which is operated by the Jet Propulsion Laboratory, California Institute of Technology, under contract with the National Aeronautics and Space Administration and the SIMBAD database, operated at CDS, Strasbourg, France.

REFERENCES

- Bennett C.L., *et al.*, 2003, *ApJS*, 148, 1
 Bouchet F.R., Gispert R., 1999, *NewA*, 4, 443
 Branchini E., *et al.*, 1999, *MNRAS*, 308, 1
 Bunn E., Fisher K.B., Hoffman Y., Lahav O., Silk J., Zaroubi S., 1994, *ApJ*, 432, L75
 Cambrésy L., Jarrett T.H., Beichman C.A., 2005, *A&A*, 435, 131
 Cardelli J.A., Clayton G.C., Mathis J.S., 1989, *ApJ*, 345, 245
 Cohen M., Wheaton W.A., Megeath S.T., 2003, *AJ*, 126, 1090
 Cole S., *et al.*, 2005, *MNRAS*, 362, 505
 Conway E., *et al.*, 2005, *MNRAS*, 356, 456
 Cooray A., Sheth R., 2002, *Physics Reports*, 372, 1
 Courteau S., Van Den Bergh S., 1999, *AJ*, 118, 337
 Davis M., Nusser A., Willick J., 1996, *ApJ*, 473, 22
 Dressler A., Faber S. M. 1990, *ApJ*, 354, L45
 Ebeling H., Mullis C.R., Tully R.B., 2002, *ApJ*, 580, 774
 Einasto M., Tago E., Jaaniste J., Einasto J., Andernach H., 1997, *A&AS*, 123, 119
 Erdoğdu P., *et al.*, 2004, *MNRAS*, 352, 939
 Erdoğdu P., *et al.*, 2006, *MNRAS*, in press
 Fabbri R. & Natale V., 1990, *ApJ*, 363, 3
 Fairall A.P., 1988, *MNRAS*, 230, 69
 Fisher K.B., Scharf C.A., Lahav O., 1994, *MNRAS*, 266, 219
 Fisher K.B., Lahav O., Hoffman Y., Lynden-Bell D., Zaroubi S., 1995, *MNRAS*, 272, 885 (FLHLZ)
 Freedman W.L., *et al.*, 2001, *ApJ*, 553, 47
 Frith W.J., Outram P.J., Shanks T., 2005, *MNRAS*, 364, 593
 Geller M., Huchra J.P., 1989, *Science*, 246, 897
 Hamilton A.J.S., Tegmark M., Padmanabhan N., 2000, *MNRAS*, 317, L23

- Heavens A.F., Taylor A.N., 1995, MNRAS, 275, 483
- Huchra J., Jarrett T.H., Skrutskie M., Cutri R., Schneider S., Macri L., Steining R., Mader J., Martinbeau N., George T., 2005, in Nearby Large-Scale Structures and the Zone of Avoidance ASP Conference Series, eds. K.P. Fairall, P.A. Woudt, 329, 135
- Hoffman Y., Eldar A., Zaroubi S., Dekel A., 2001, astro-ph/0102190
- Jarrett T.H., Chester T., Cutri R., Schneider S.E., Skrutskie M. & Huchra J.P., 2000a, AJ, 119, 2498
- Jarrett T.H., Chester T., Cutri R., Schneider S.E., Rosenberg J., & Huchra J.P., 2000b, AJ, 120, 298
- Jarrett T.H., Chester T., Cutri R., Schneider S.E. & Huchra J.P., 2003, AJ, 125, 525
- Jarrett T.H., 2004, PASA, 21, 396
- Jones D. H. *et al.* , 2004, MNRAS, 355, 747
- Jones D. H. *et al.* , 2004, PASA, 22, 277
- Klemola A.R., 1969, AJ, 74, 804
- Kochanek C.S., *et al.* , 2001, ApJ, 560, 566
- Kraan-Korteweg R.C., Woudt P.A., Cayette V., Fairall A.P., Balkowski C., Henning P.A., 1996, Nature, 379, 519
- Lahav O., Yamada T., Scharf C., Kraan-Korteweg R.C., 1993, MNRAS, 262, 711
- Lahav O., Fisher K.B., Hoffman Y., Scharf C.A., Zaroubi S., 1994, ApJ, 423, L93
- Lynden-Bell D., 1993, in Statistical Challenges in Modern Astronomy, eds. Babu G.B., Feigelson E.D., Springer-Verlag, New York, p.201
- Maller A.H., McIntosh D.H., Katz N., Weinberg M.D., 2005, ApJ, 619, 147
- Marinoni C. *et al.* , 2005, A&A, 442, 801
- Mathewson D.S., Ford V.L., Buchhorn M., 1992, ApJ, 389, L5
- Nusser A., Davis M., 1994, ApJ, 421, L1
- Peacock J.A., Dodds S., 1994, MNRAS, 267, 1020
- Peebles P.J.E., 1973, ApJ, 185, 413
- Peebles P.J.E., 1980, The Large-Scale Structure of the Universe, Princeton University Press, Princeton, NJ
- Pike R.W., Hudson M.J., 2005, ApJ, 635, 11
- Porter S.C., Raychaudhury S., 2005, MNRAS, 364, 1387
- Press W.H., Vetterling W.T., Teukolsky S.A., Flannery B. P., 1992, Numerical Recipes in Fortran 77, 2nd edn., Cambridge University Press, Cambridge, UK
- Rassat A., *et al.* 2006, in preparation
- Regős E., Szalay A.S., 1989, ApJ, 345, 627
- Rybicki G.B., Press, W.H., 1992, ApJ, 398, 169
- Rowan-Robinson M., *et al.* 2000, MNRAS, 314, 375
- Saunders W., *et al.* , 2000, MNRAS, 317, 55
- Saunders W., Frenk C., Rowan-Robinson M., Efstathiou G., Lawrence A., Kaiser N., Ellis R., Crawford J, Xia X-Y, Parry I., Nature, 1991, 349, 32
- Scharf C.A., Hoffman Y., Lahav O., Lynden-Bell D., 1992, MNRAS, 256, 229
- Scharf C.A., Lahav O., 1993, MNRAS, 264, 439
- Schlegel D.J., Finkbeiner D.P., Davis M., 1998, ApJ, 500, 525
- Schmoldt I.M., *et al.* , 1999, AJ, 118, 1146
- Spergel D.N., *et al.* , 2006, submitted to ApJ
- Tadros H., *et al.* , 1999, MNRAS, 305, 527
- Taylor A.N., Ballinger W.E., Heavens A.F., Tadros H., 2001, MNRAS, 327, 689
- Tegmark M., Efstathiou G., 1996, MNRAS, 281, 1297.
- Tegmark M., *et al.* , 2004, ApJ, 606, 70
- Valentine H., Saunders W., Taylor A., 2000, MNRAS, 319, L13
- Webster M., Lahav O., Fisher K., 1997, MNRAS, 287, 425 (WLF)
- Wegner G., Colless M., Saglia R.P., McMahan R., Davies R.L., Burstein D., Baggle G., 1999, MNRAS, 305, 259
- White R.A., Bliton M., Bhavsar S.P., Bornmann P., Burns J., Ledlow M., Loken C., 1999, AJ, 118, 2014
- Wiener N., 1949, in Extrapolation and Smoothing of Stationary Time Series with Engineering Applications, Technology Press of MIT, Cambridge, MA
- Wild V., *et al.* , 2005, MNRAS, 356, 247
- Worthey G., 1994, ApJS, 95, 107
- Woudt P., 1998, PhD thesis, Cape Town University
- Yahil A., Strauss M., Davis M., Huchra J.P., 1991, ApJ, 372, 380
- Yahil A., 1994, in Evolution of the Universe and its Observational Quest, ed. K. Suto, Tokyo Universal Academy Press, Japan
- Zaroubi S., Hoffman, Y., Fisher, K., and Lahav, O., 1995, ApJ, 449, 446
- Zaroubi S., Hoffman, Y., 1996, ApJ, 462, 25
- Zaroubi S., 2002, MNRAS, 331, 901
- Zwicky F., Herzog E., 1966, Catalogue of Galaxies and of Clusters of Galaxies, Vol III, California Institute of Technology, Pasadena, CA